Supplementary Information

Atomic-scale built-in electric field imaging reveals Fe-O_v synergistic enhancement of charge migration for electrocatalyst

Bowen Shi[1,2 †], Zhuang Zhang[3, †], Yue Gao[1,2], Shaowen Xu[3], Liu Zhu[2], Nan Zhang[3], Pinxian Xi[3], Yang Hu[1,2]*, and Yong Peng[1,2]*

[1] School of Materials and Energy of Lanzhou University, Lanzhou 730000, China.

[2] Electron Microscopy Centre of Lanzhou University, Lanzhou 730000, China.

[3] College of Chemistry and Chemical Engineering, Frontiers Science Center for Rare Isotopes, Lanzhou University, Lanzhou 730000, China.

*e-mail: yang_hu@lzu.edu.cn; pengy@lzu.edu.cn

[†]These authors contributed equally.

Contents

Experimental section

Materials. Nickel nitrate hexahydrate ($Ni(NO_3)_2·6H_2O$, 98.0%), cobalt (II) nitrate hexahydrate ($Co(NO_3)_2·6H_2O$, 99.0%), ferric nitrate nonahydrate ($Fe(NO_3)_3·9H_2O$, 98.0%), urea (99.0%), and potassium hydroxide (KOH, 90.0%) were purchased from Aladdin, and the electrodes were obtained from Coats & Reed. Deionized (DI) water for solution preparation was obtained from Millipore Autopure system (18.2 MΩ, Millipore Ltd, USA). For electrochemical experiments, 1 M KOH was used as the supporting electrolyte. All other chemicals and reagents used for electrochemical measurements were of analytical grade and used as is.

Synthesis of $NiCo_2O_x$ nanocrystals. The synthesis of $NiCo_2O_x$ nanocrystals was initiated by dissolving stoichiometric amounts of $Ni(NO_3)_2·6H_2O$ (0.33 g), $Co(NO_3)_2·6H_2O$ (0.665 g), and urea (0.24 g) in 80 mL of deionized water under continuous magnetic stirring for 30 minutes. The homogeneous solution was subsequently transferred into a 100 mL PTFE-lined autoclave and subjected to hydrothermal treatment at 120 °C for 16 hours. Following the reaction, the resulting precipitate was collected and thermally treated at 300 °C overnight with a controlled heating ramp of 2 °C/min. The intermediate product was then isolated via centrifugation at 8000 rpm for 5 minutes, followed by sequential washing with deionized water and absolute ethanol. After drying at 60 °C for 12 hours, the material was calcined in air at 300 °C for 2 hours (heating rate: 2 °C/min) to yield the final $NiCo_2O_x$ nanocrystals.

The synthesis of $NCFO_x$ was carried out as above, requiring only the proportional addition of $Fe(NO_3)_3·9H_2O$.

Synthesis of $NCFO_x$, NCO_δ, and $NCFO_\delta$. The synthesis of $NiCo_2O_x$ precursors is detailed in the experimental section of the Supplementary Information, and the synthesis of Fe-doped $NCFO_x$ catalysts was achieved by the proportional addition of hydrated iron nitrate to the feedstock. And then the catalysts NCO_x and $NCFO_x$ were placed in a crucible, and the reaction tube was heated up to 400 °C at a heating rate of 2 °C min^{-1} in a flowing N_2 atmosphere, held for 2 h, and finally cooled down in a flowing N_2 atmosphere to obtain NCO_δ and $NCFO_\delta$ nanomaterials, respectively.

Electrochemical measurements. The electrochemical tests were performed in a standard three-electrode system using a CHI 760E electrochemical analysis system (Shanghai Chenhua Instrument Co., Ltd.). The electrolyte was 1.0 M KOH solution, and the temperature was precisely controlled by

a thermostat at 20.0±0.2°C. The counter electrode was made of platinum foil, and the reference system was mercury/mercury oxide electrode (Hg/HgO) filled with 1.0 M KOH, and all the potentials were calibrated with the reversible hydrogen electrode (RHE) as the reference. The working electrode was prepared from a 3 mm diameter glassy carbon electrode with surface modification. The catalyst ink was prepared by dispersing 3 mg of catalyst in 1450 μL of *N, N*-dimethylformamide (DMF) and 50 μL of 5 wt % Nafion solution. Then, 7.1 μL of catalyst ink was loaded onto the surface glassy carbon electrode (mass loading: 0.02 mg/cm^2) and air-dried at room temperature.

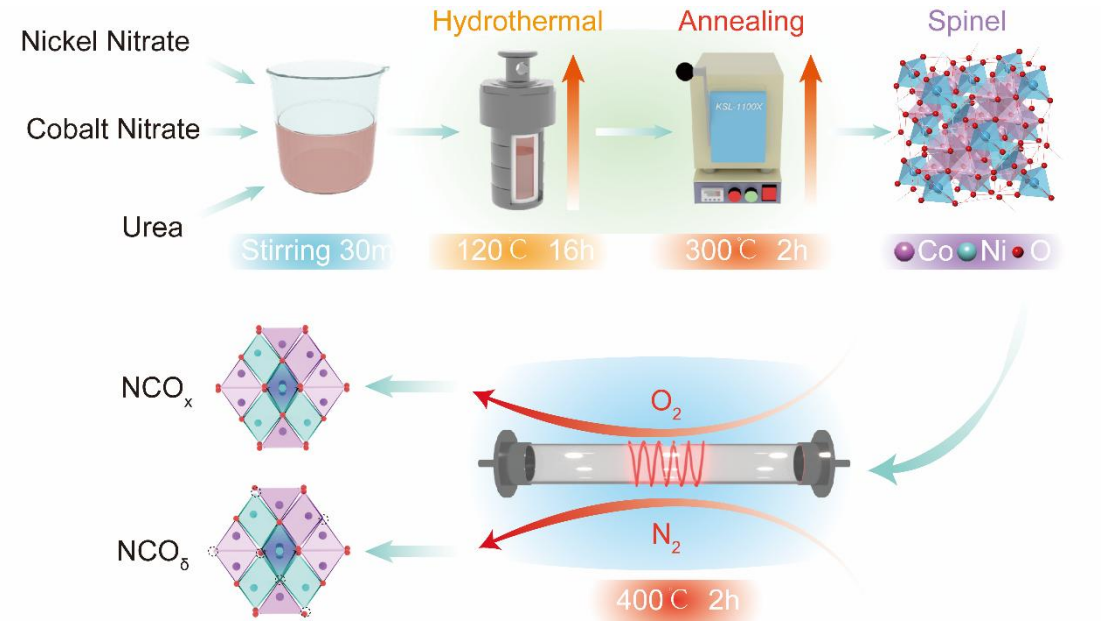

Supplementary Fig. 1 | Material synthesis. Schematic diagram of the synthesis strategy for $NiCo_2O_x$ and $NiCo_2O_\delta$ spinel.

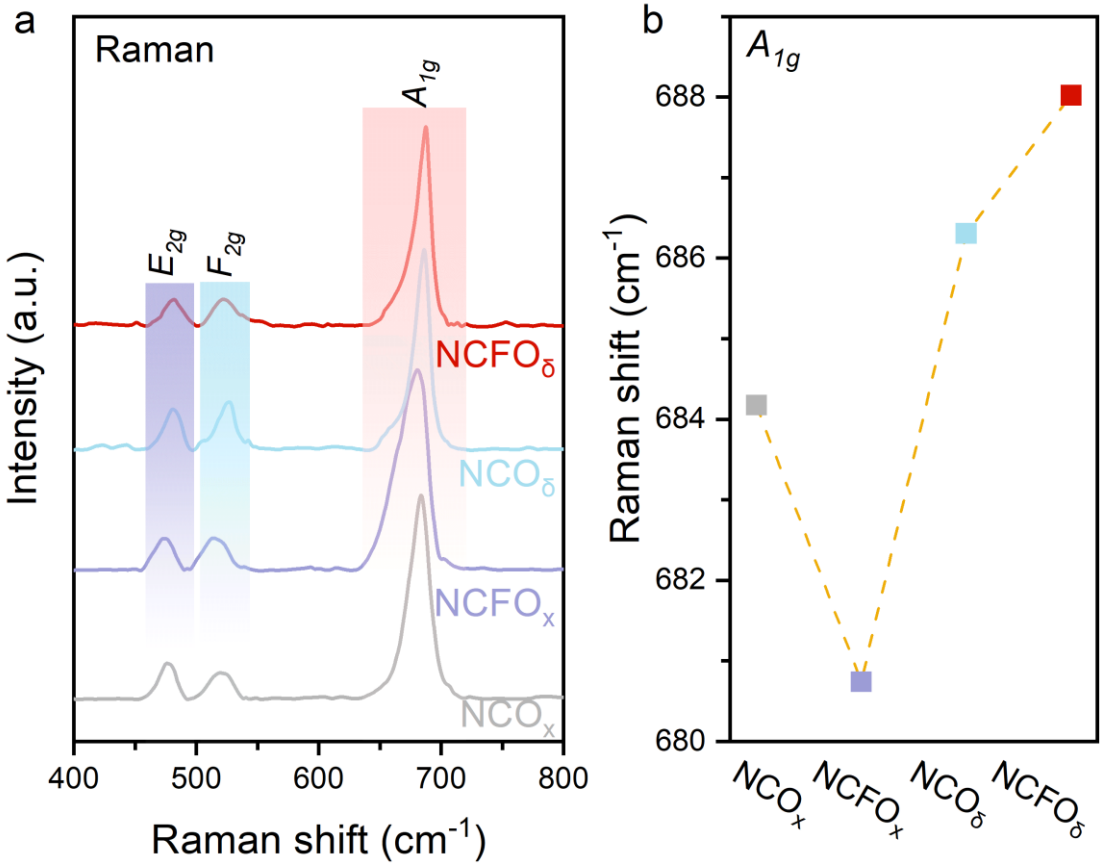

Supplementary Fig. 2 | Raman spectra of catalytic materials. a. Spectra in the 400 cm^{-1}-800 cm^{-1} Raman shift interval. **b.** Peak position comparison of A_{1g} characteristic Raman peaks of catalyst materials.

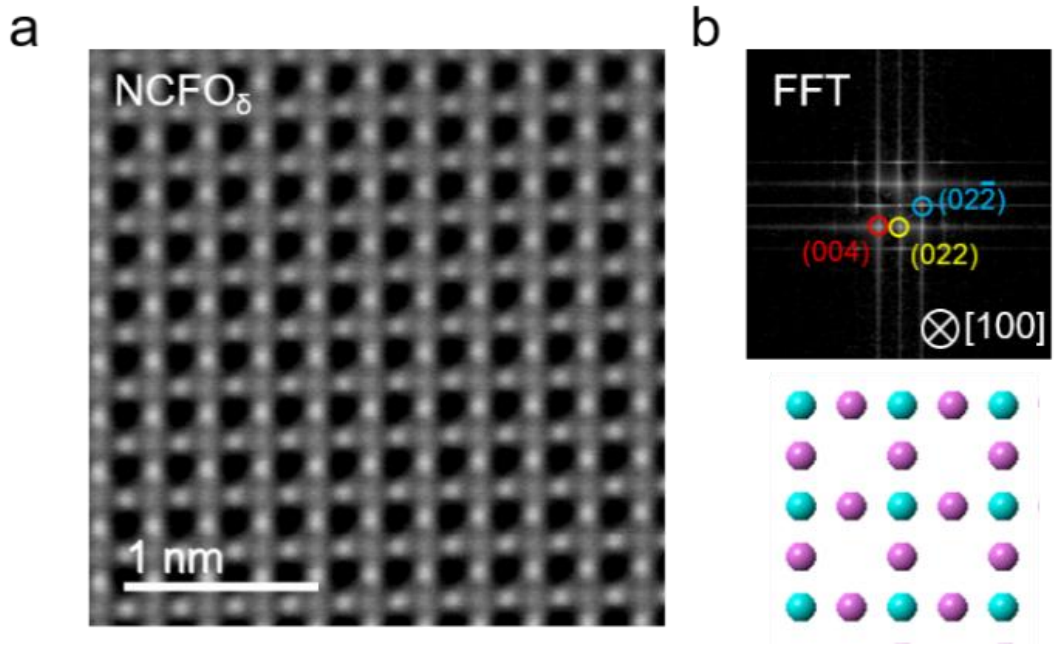

Supplementary Fig. 3 | Structural characterization of NCFO$_\delta$. a. Atomic STEM-HAADF image of NCFO$_\delta$. **b.** Corresponding FFT pattern along [100] orientation.

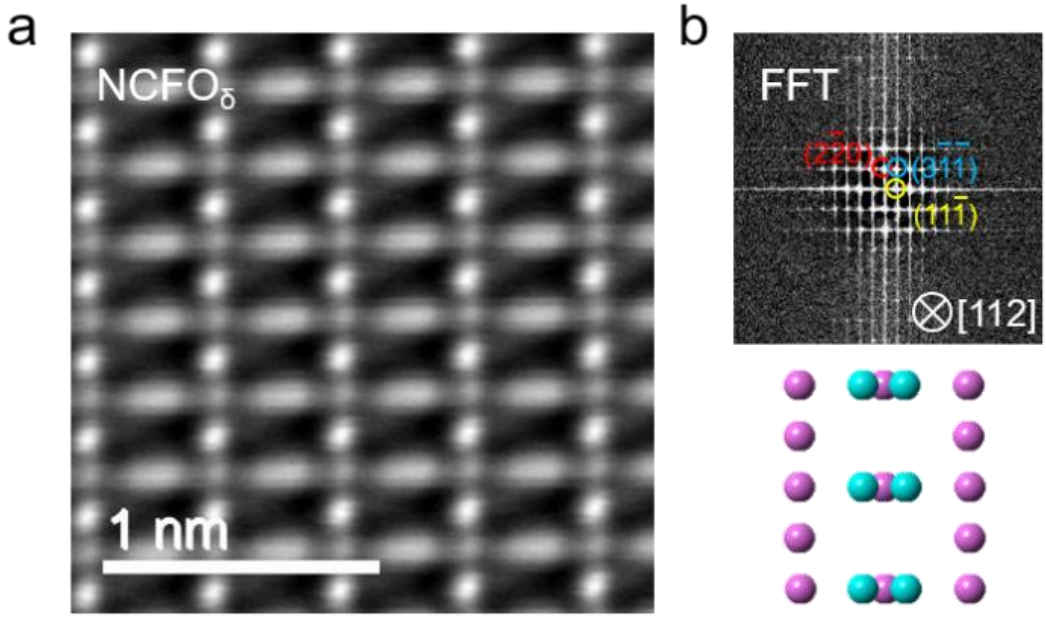

Supplementary Fig. 4 | Structural characterization of NCFO$_\delta$. a. Atomic STEM-HAADF image of NCFO$_\delta$. **b.** Corresponding FFT pattern along [112] orientation.

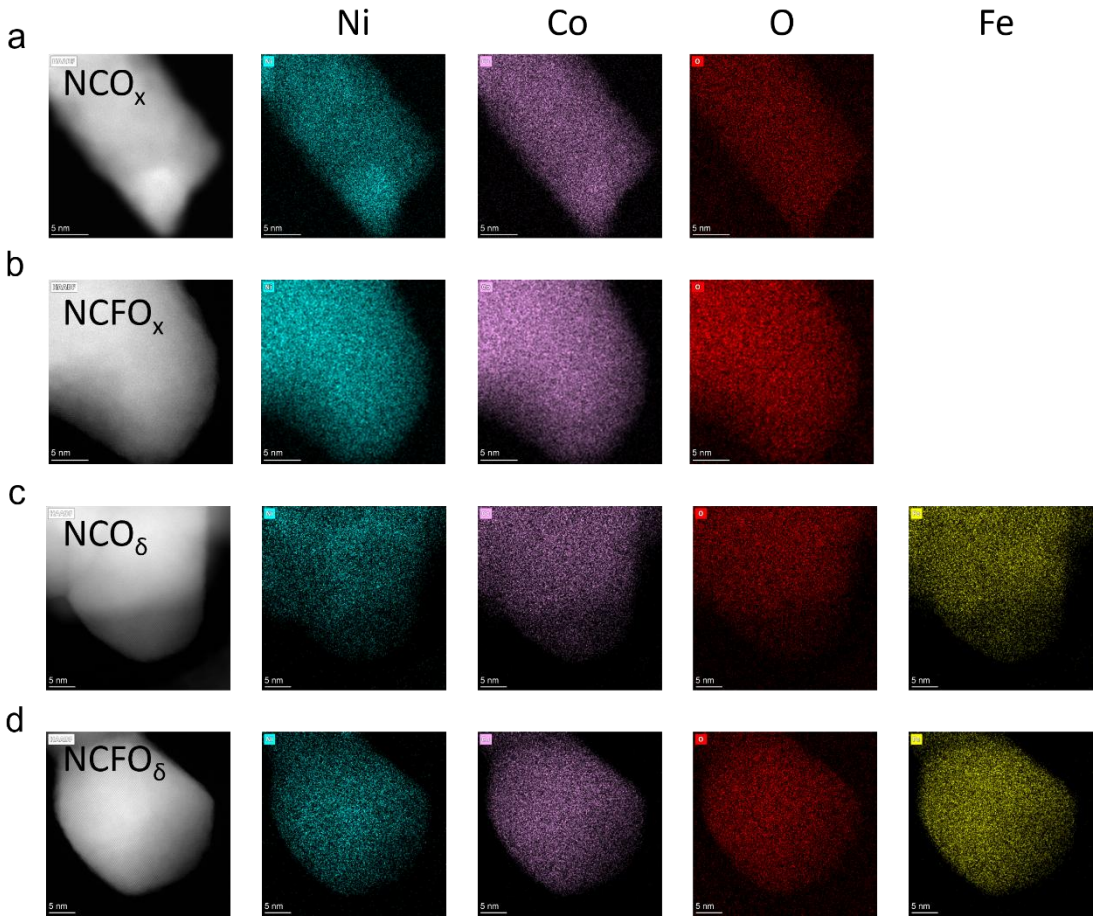

Supplementary Fig. 5 | EDX elemental mapping of the catalysts. a. NCO_x **b.** $NCFO_x$ **c.** NCO_δ **d.** $NCFO_\delta$.

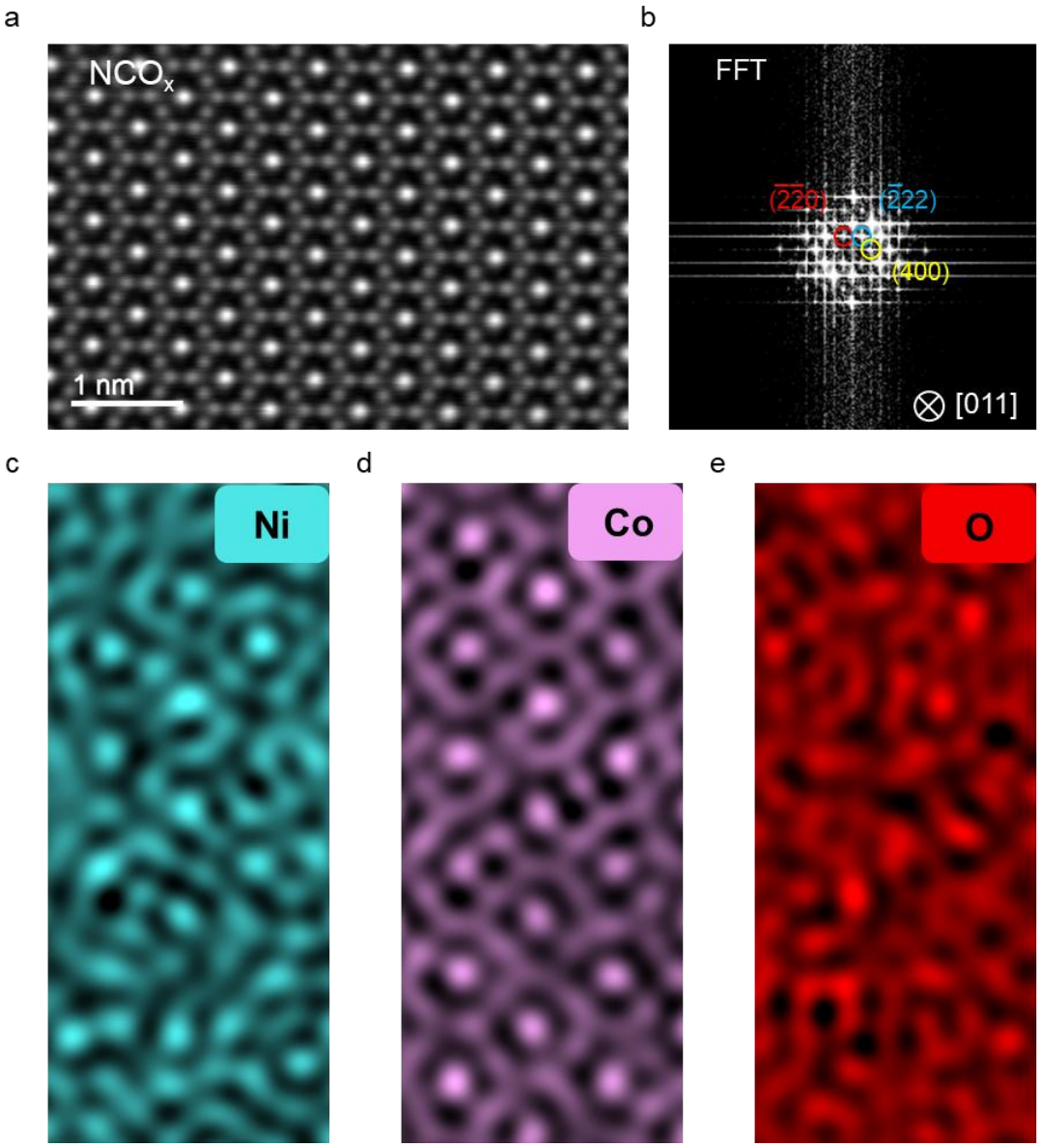

Supplementary Fig. 6 | Structural characterization of NCO_x. a. Atomic STEM-HAADF image of NCO_x. **b.** Corresponding FFT pattern along [011] orientation. **c-e** Atomic EDX elemental mapping of Ni, Co and O.

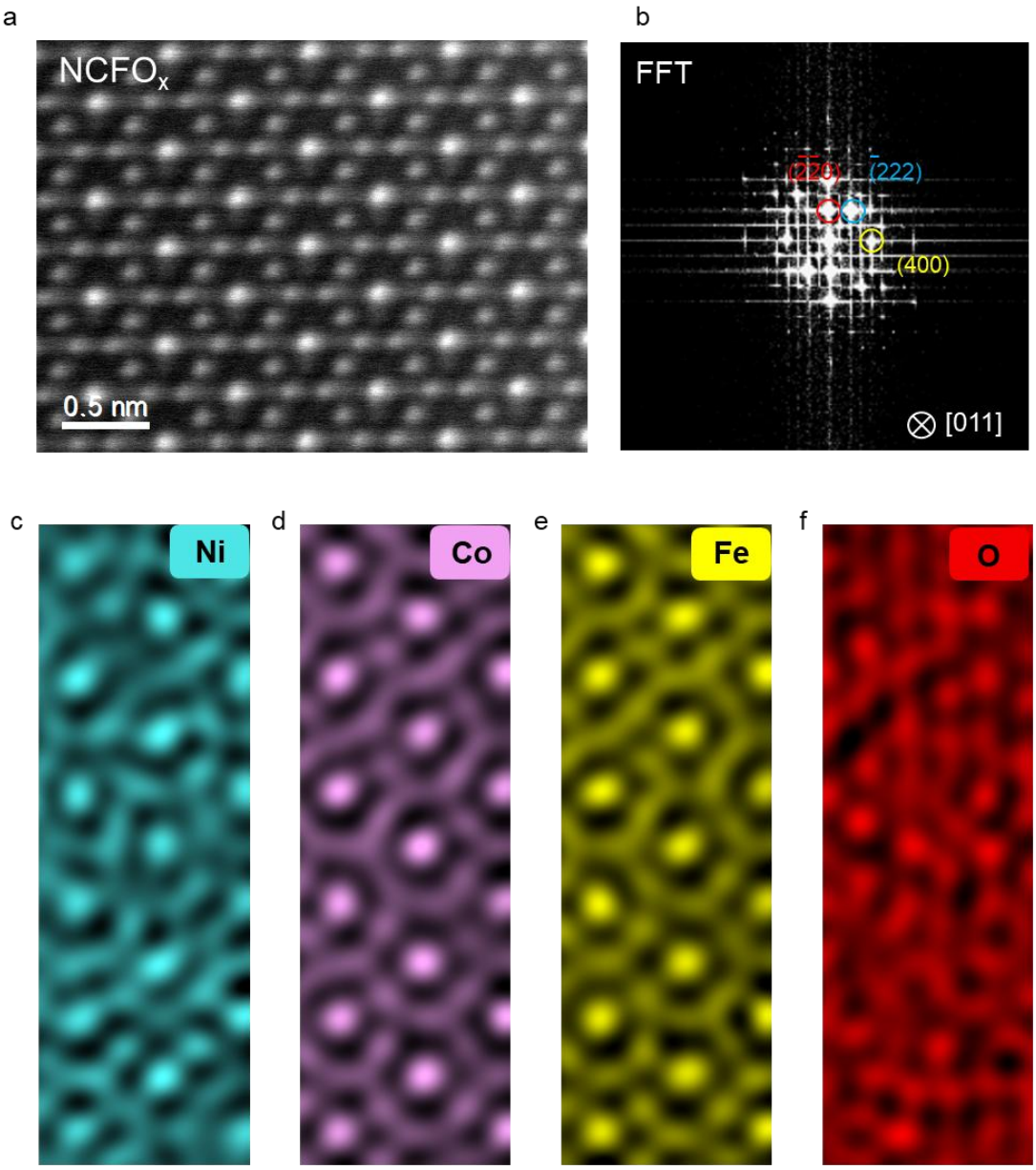

Supplementary Fig. 7 | Structural characterization of NCFO$_x$. a. Atomic STEM-HAADF image of NCFO$_x$. **b.** Corresponding FFT pattern along [011] orientation. **c-f.** Atomic EDX elemental mapping of Ni, Co, Fe and O.

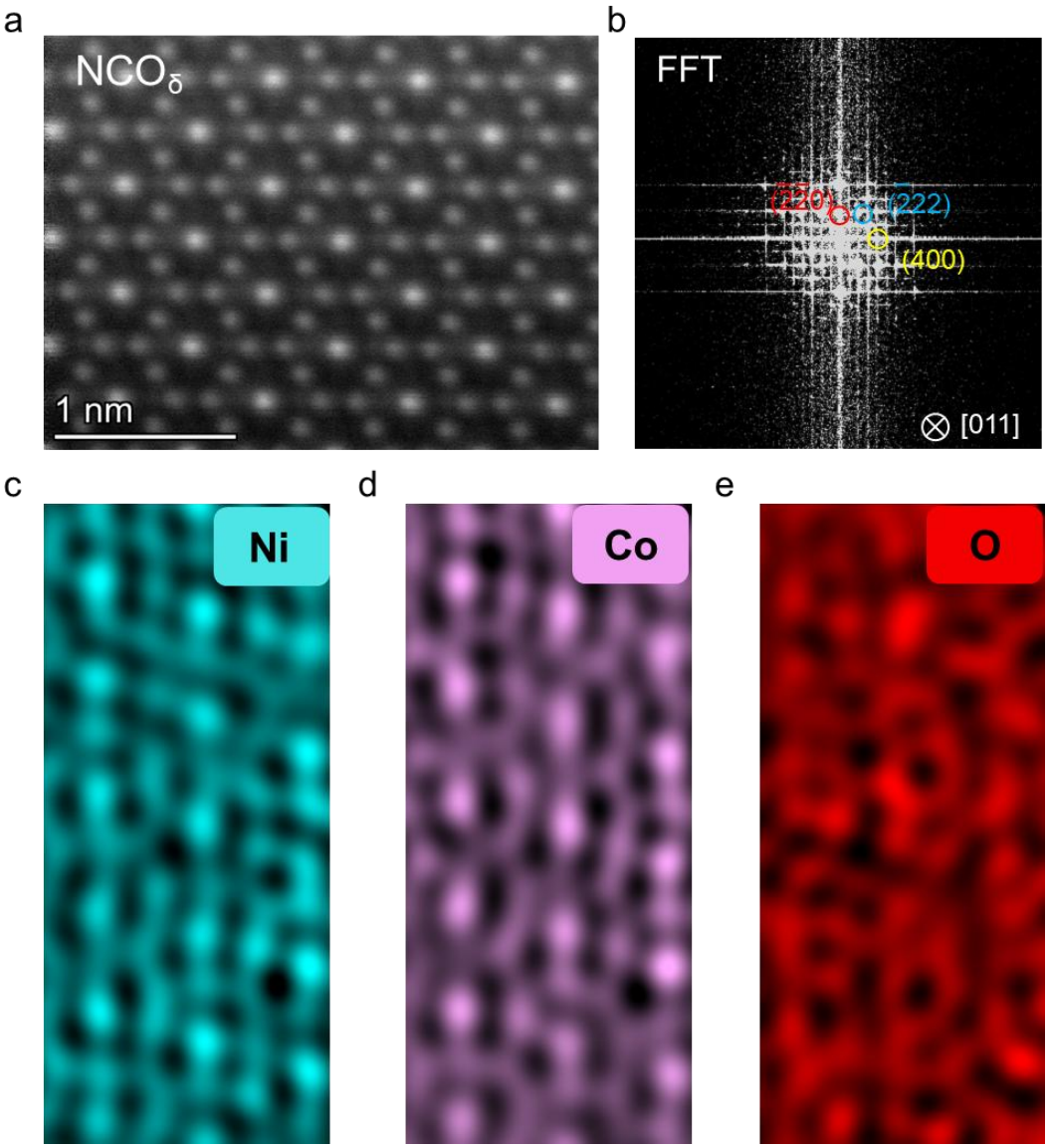

Supplementary Fig. 8 | Structural characterization of NCFO$_x$. a. Atomic STEM-HAADF image of NCFO$_x$. **b.** Corresponding FFT pattern along [011] orientation. **c-e.** Atomic EDX elemental mapping of Ni, Co and O.

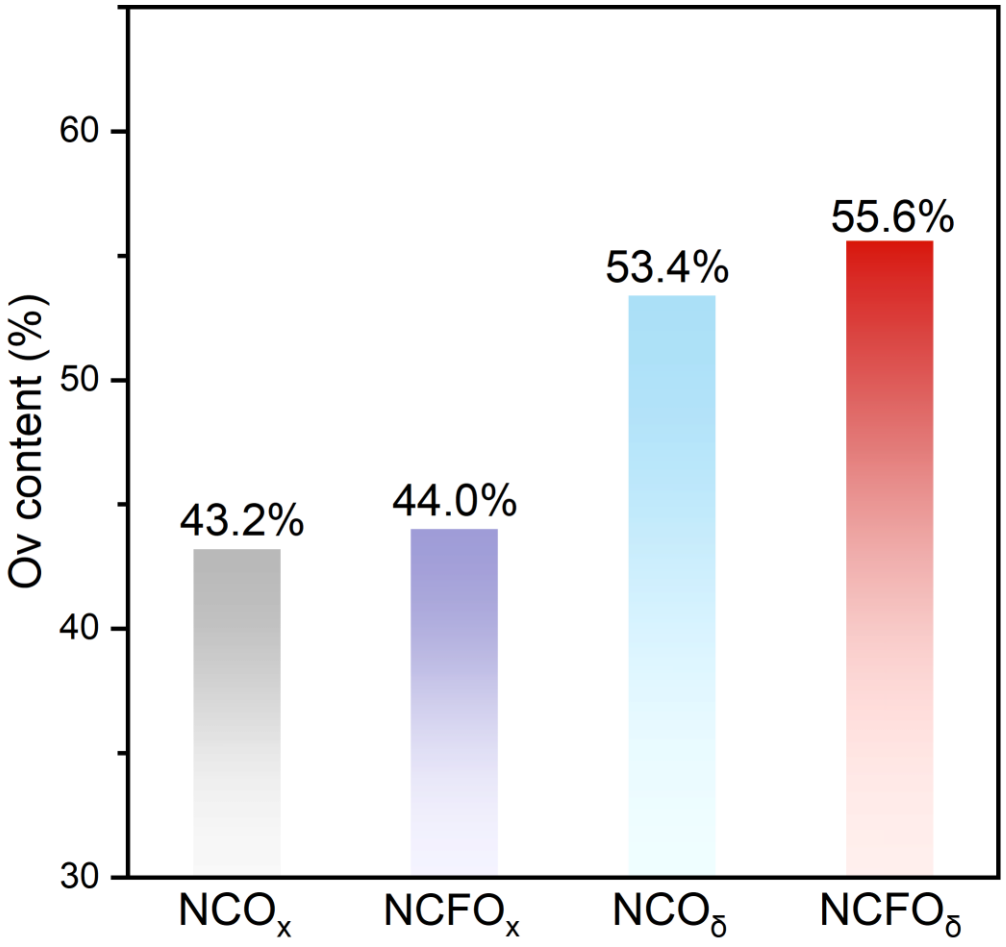

Supplementary Fig. 9 | O_v content trend obtained from XPS peak fitting.

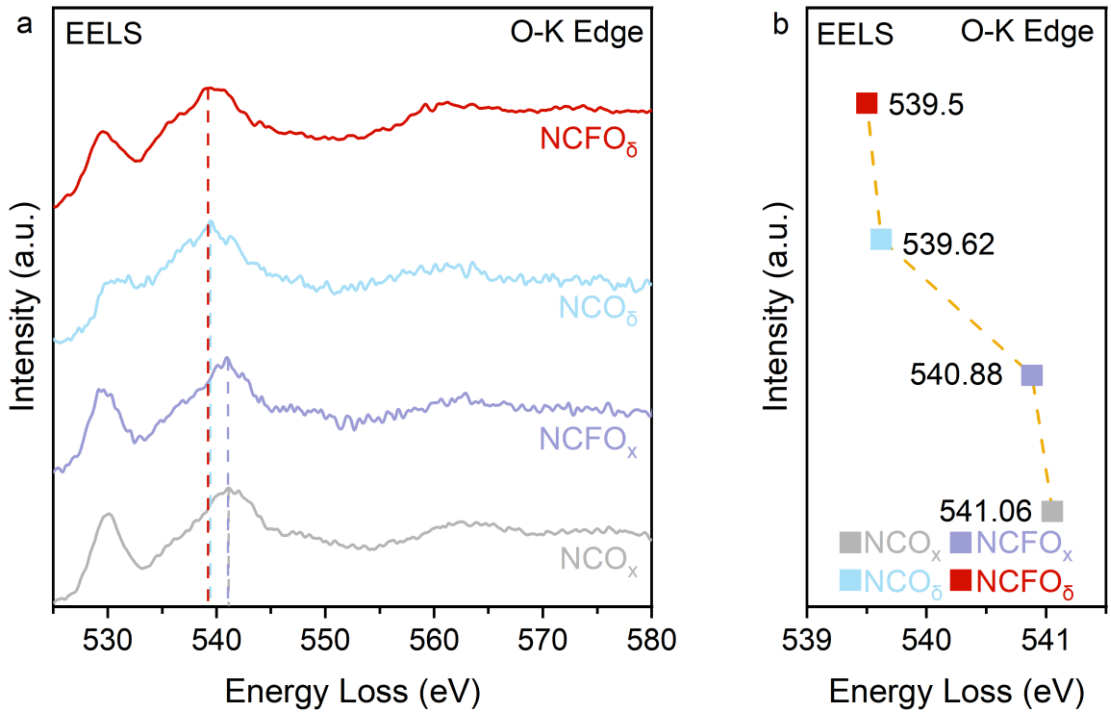

Supplementary Fig. 10 | The EELS spectra of the element O. a. O-K edge. **b.** Peak positions of O-K edge collected from EELS spectra.

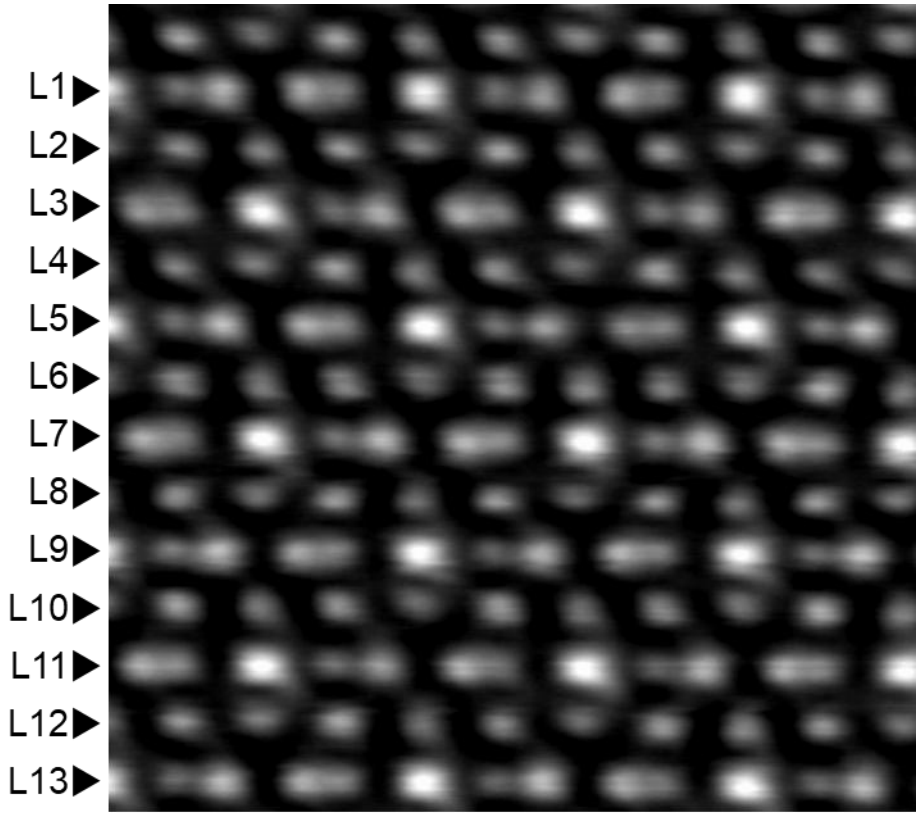

Supplementary Fig. 11 | iDPC-STEM image of $NCFO_{\delta}$. Labels L1-L13 are used to analyze atomic contrast information in each row, thereby generating atomic contrast distribution maps.

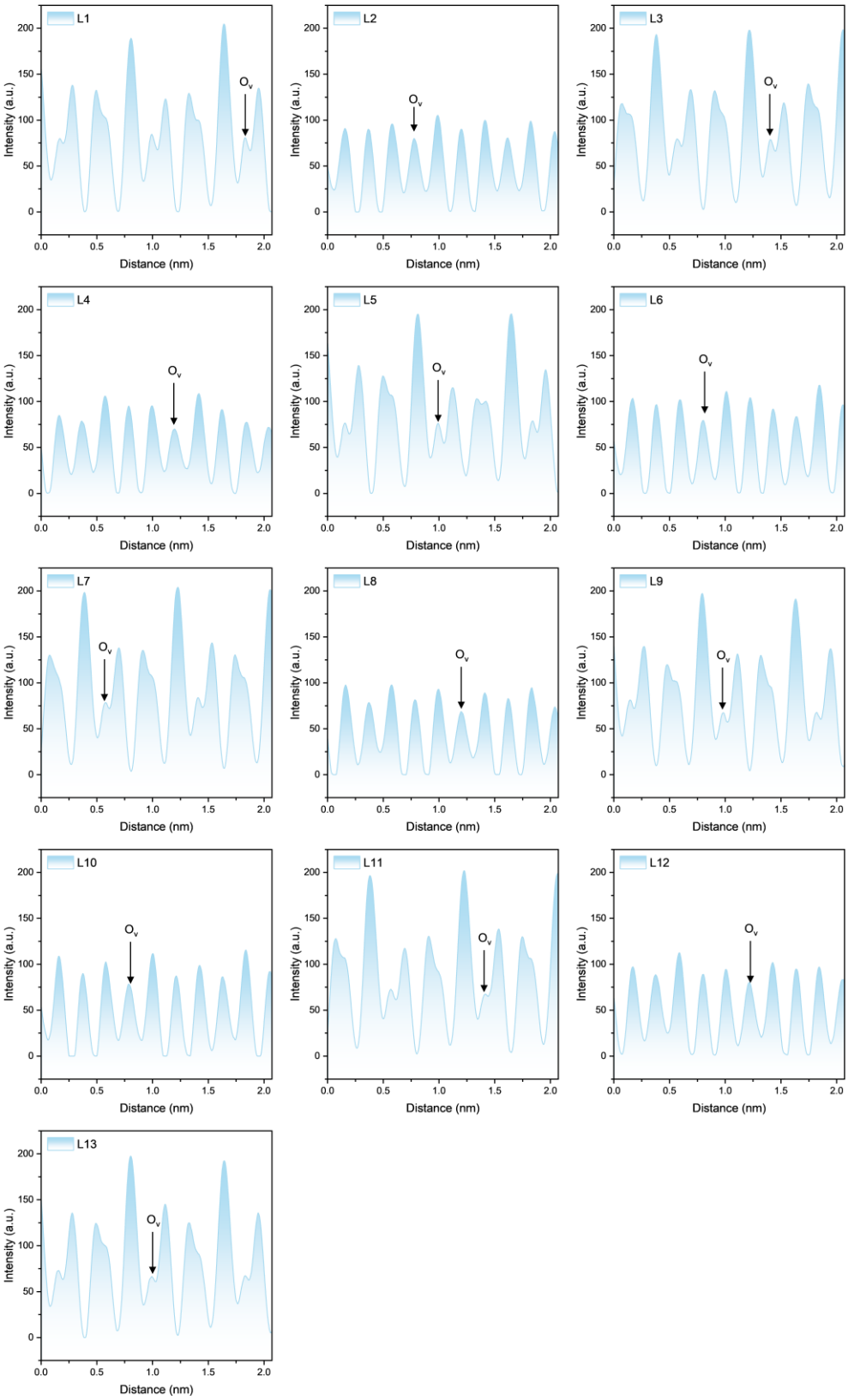

Supplementary Fig. 12 | iDPC-STEM contrast distribution map for L1–L13 obtained from Supplementary Fig. 11.

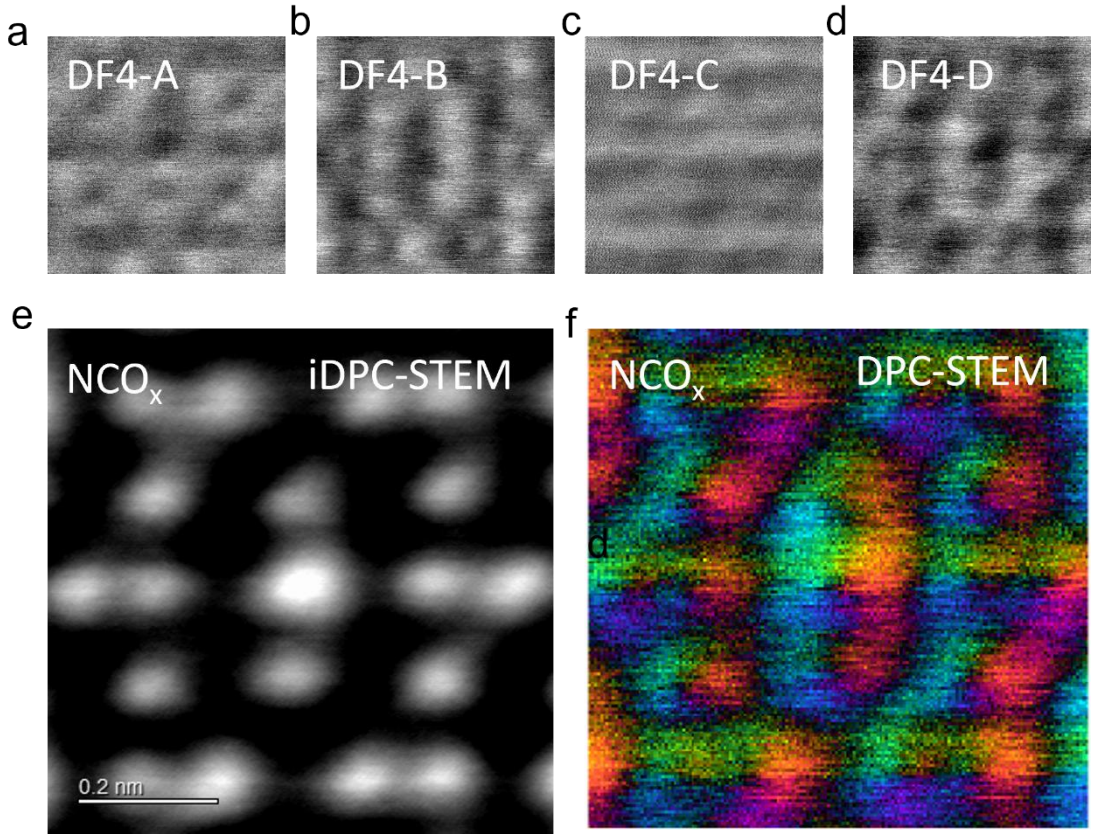

Supplementary Fig. 13 | DPC-STEM characterization of the NCO_x catalyst in the [110] direction. a–d. Images obtained from the quadrant detectors. **e.** iDPC-STEM image calculated from the quadrant detector images. **f.** DPC-STEM image calculated from the quadrant detector images.

DPC-STEM technology captures the electric field deflection signals generated by the interaction between the electron beam and the sample using a four-quadrant detector. Through sophisticated mathematical processing of the detector signals, it precisely maps the internal electric field distribution of the sample, thereby obtaining charge localization information at atomic resolution.

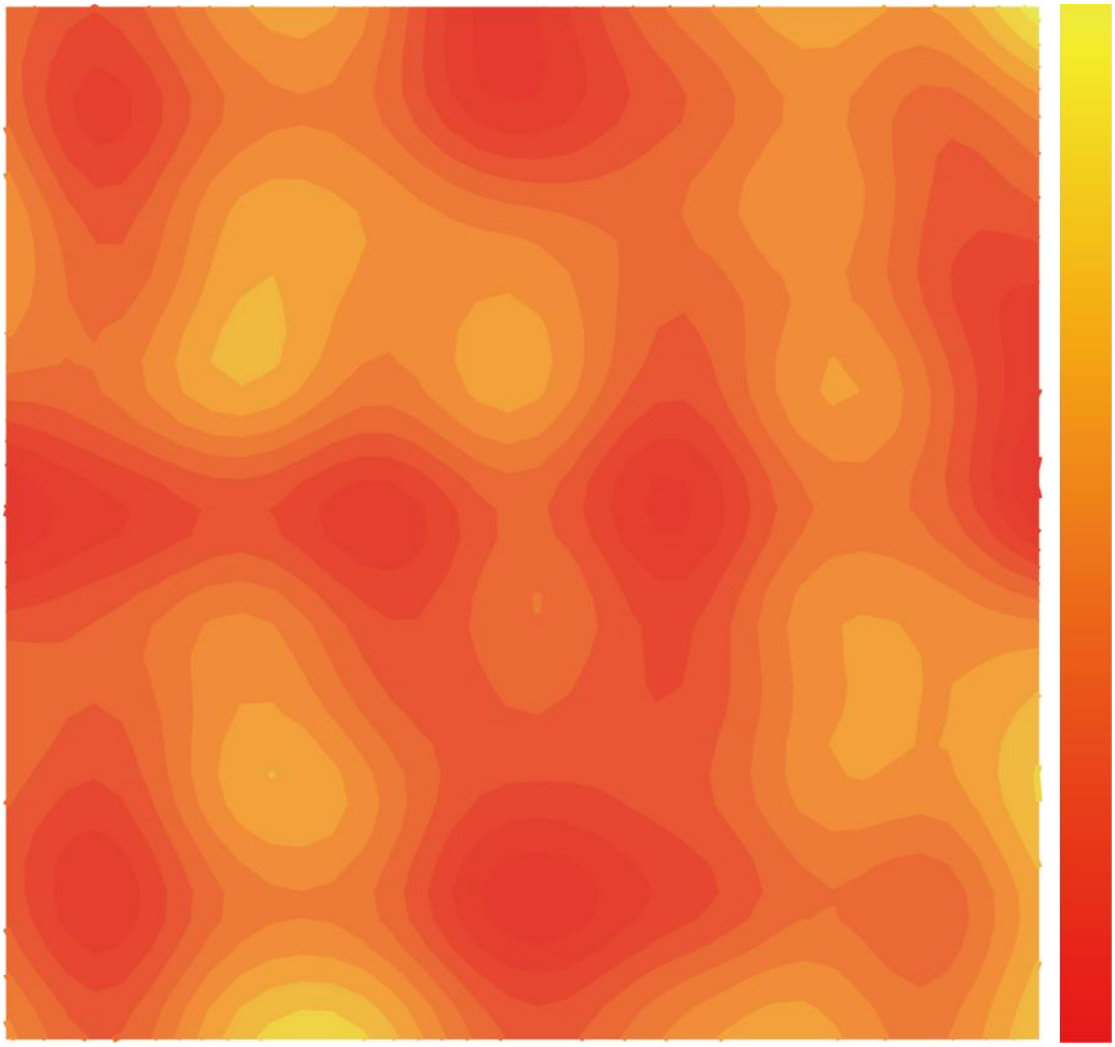

Supplementary Fig. 14 | Potential information of the catalytic material obtained via DPC-STEM corresponds to NCO_x.

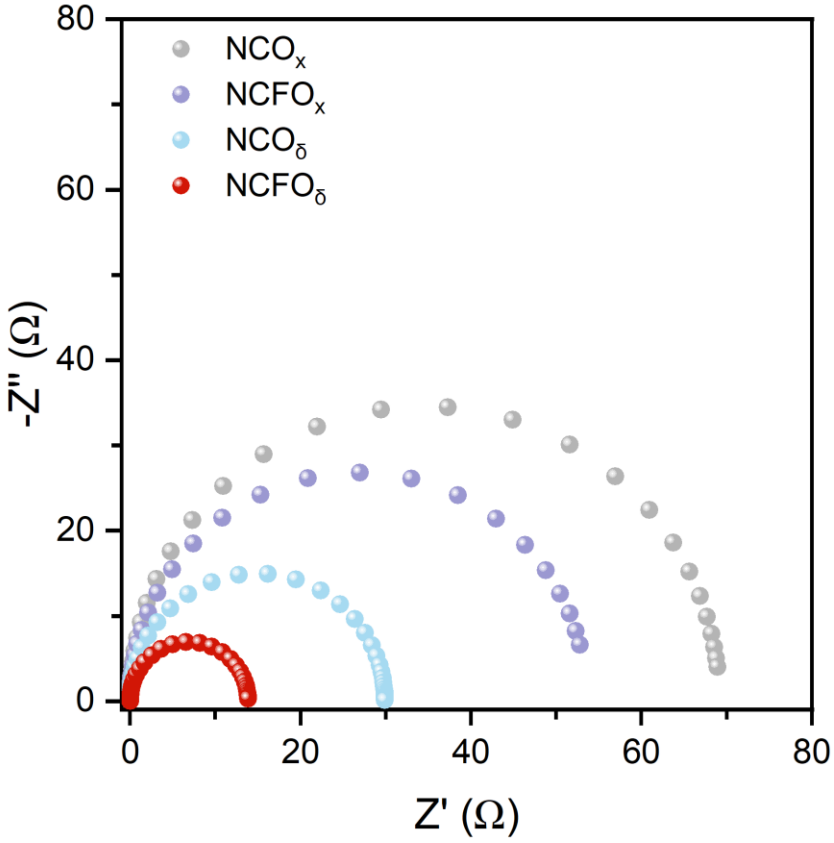

Supplementary Fig. 15 | The EIS of catalytic materials.

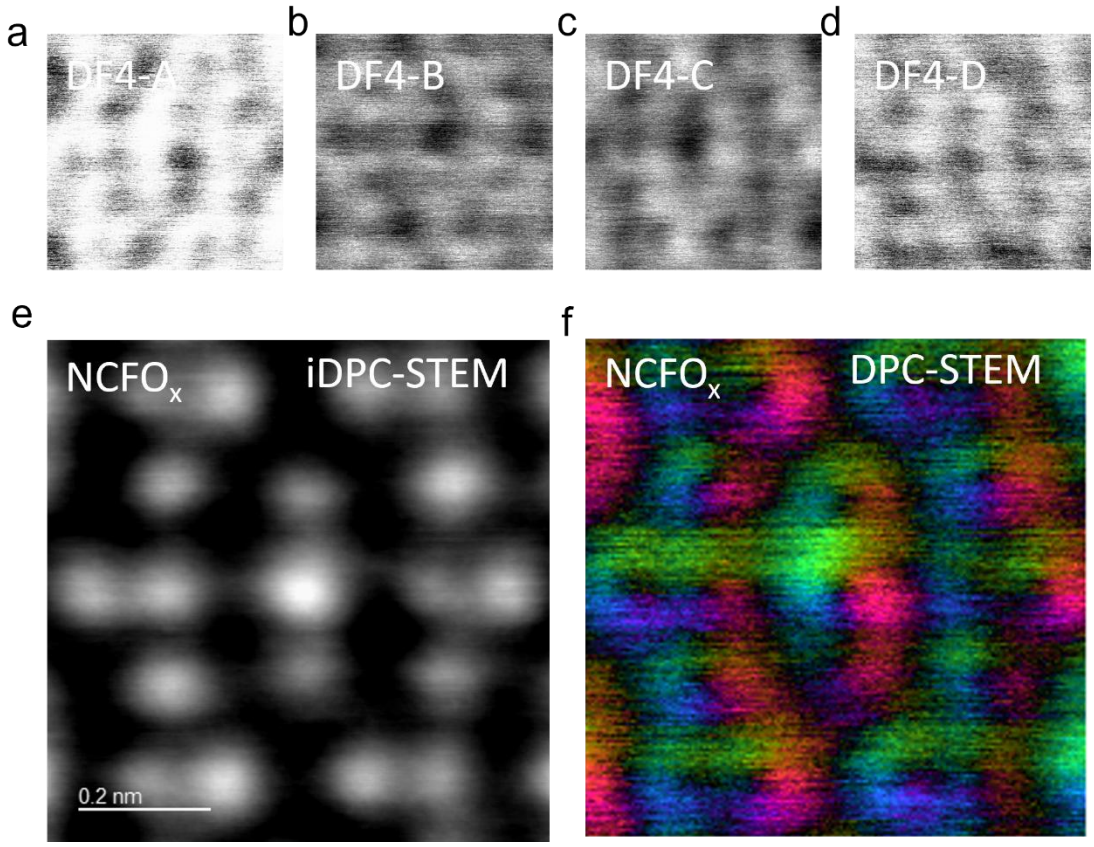

Supplementary Fig. 16 | DPC-STEM characterization of the $NCFO_x$ catalyst in the [110] direction. a–d. Images obtained from the quadrant detectors. **e.** iDPC-STEM image calculated from the quadrant detector images. **f.** DPC-STEM image calculated from the quadrant detector images.

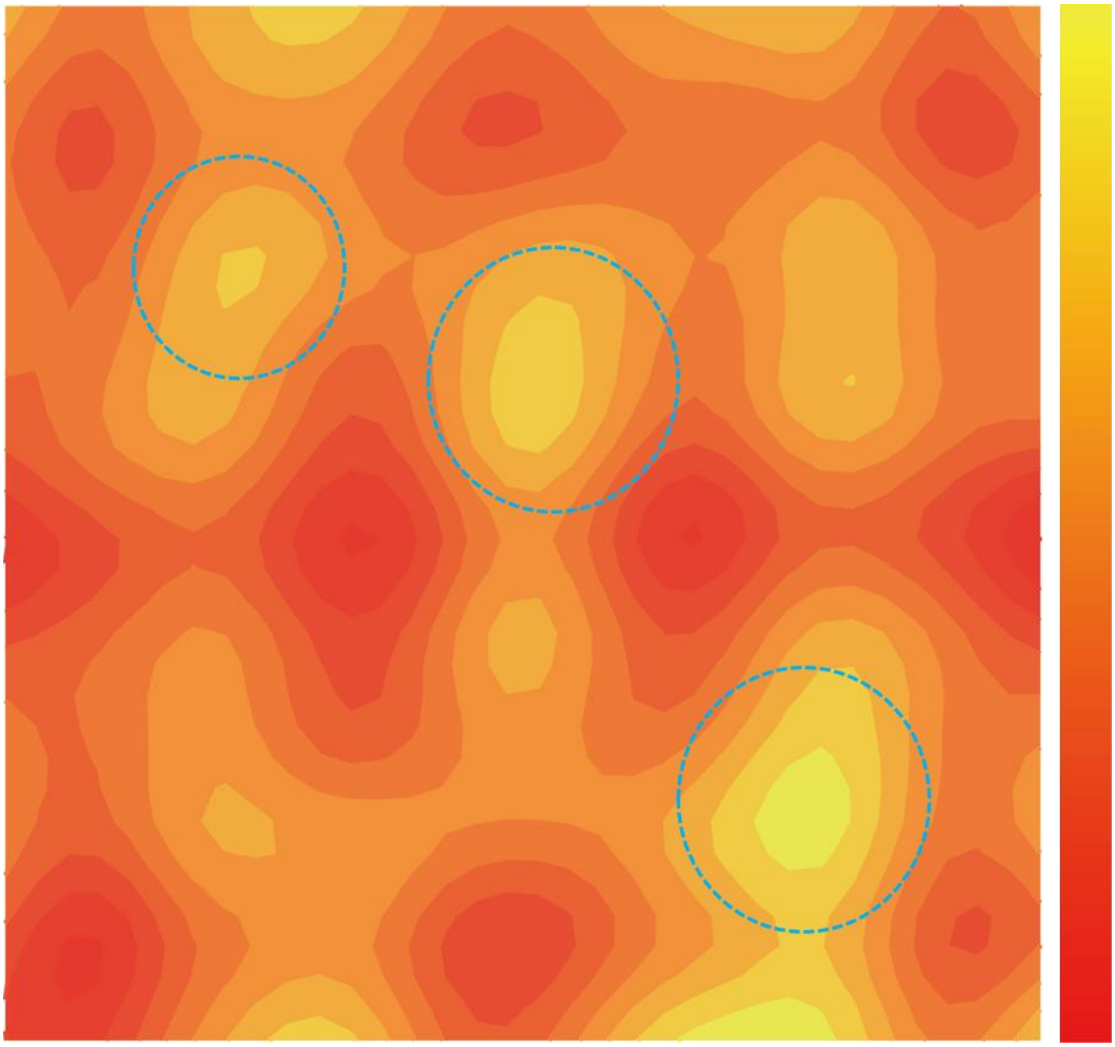

Supplementary Fig. 17 | Potential information of the catalytic material obtained via DPC-STEM corresponds to $NCFO_x$.

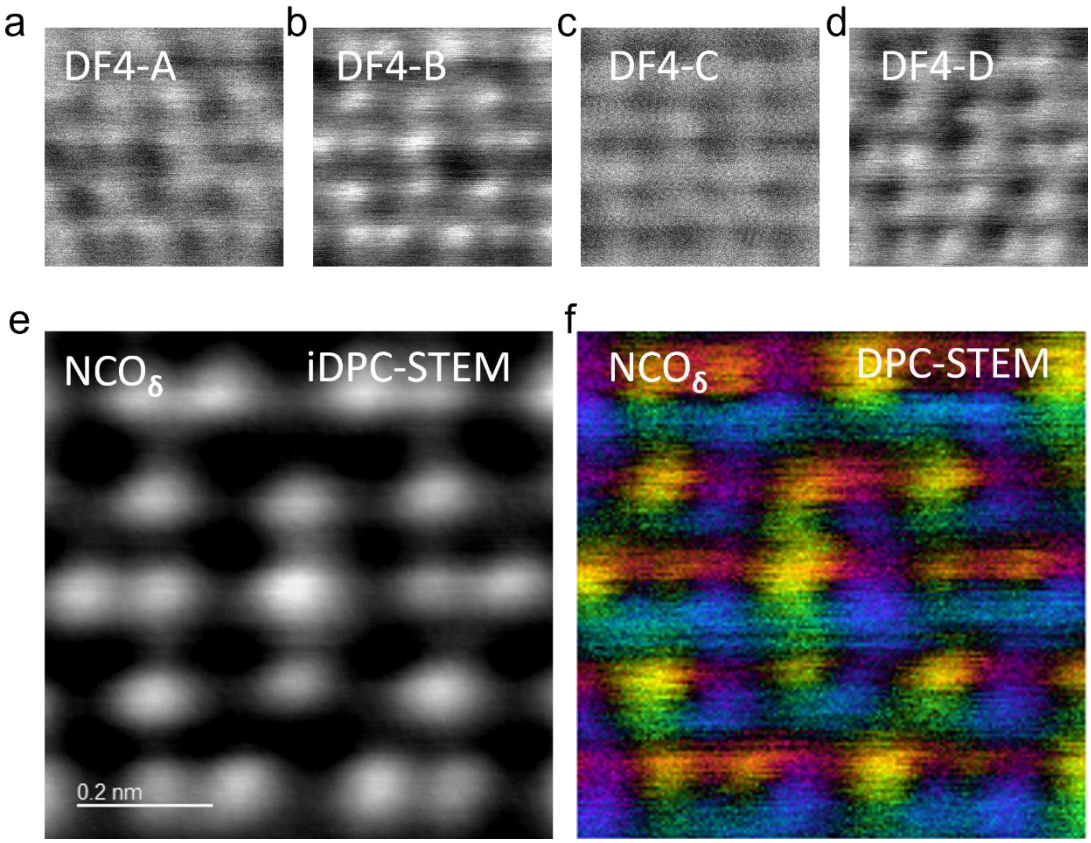

Supplementary Fig. 18 | DPC-STEM characterization of the NCO_{δ} catalyst in the [110] direction. a–d. Images obtained from the quadrant detectors. **e.** iDPC-STEM image calculated from the quadrant detector images. **f.** DPC-STEM image calculated from the quadrant detector images.

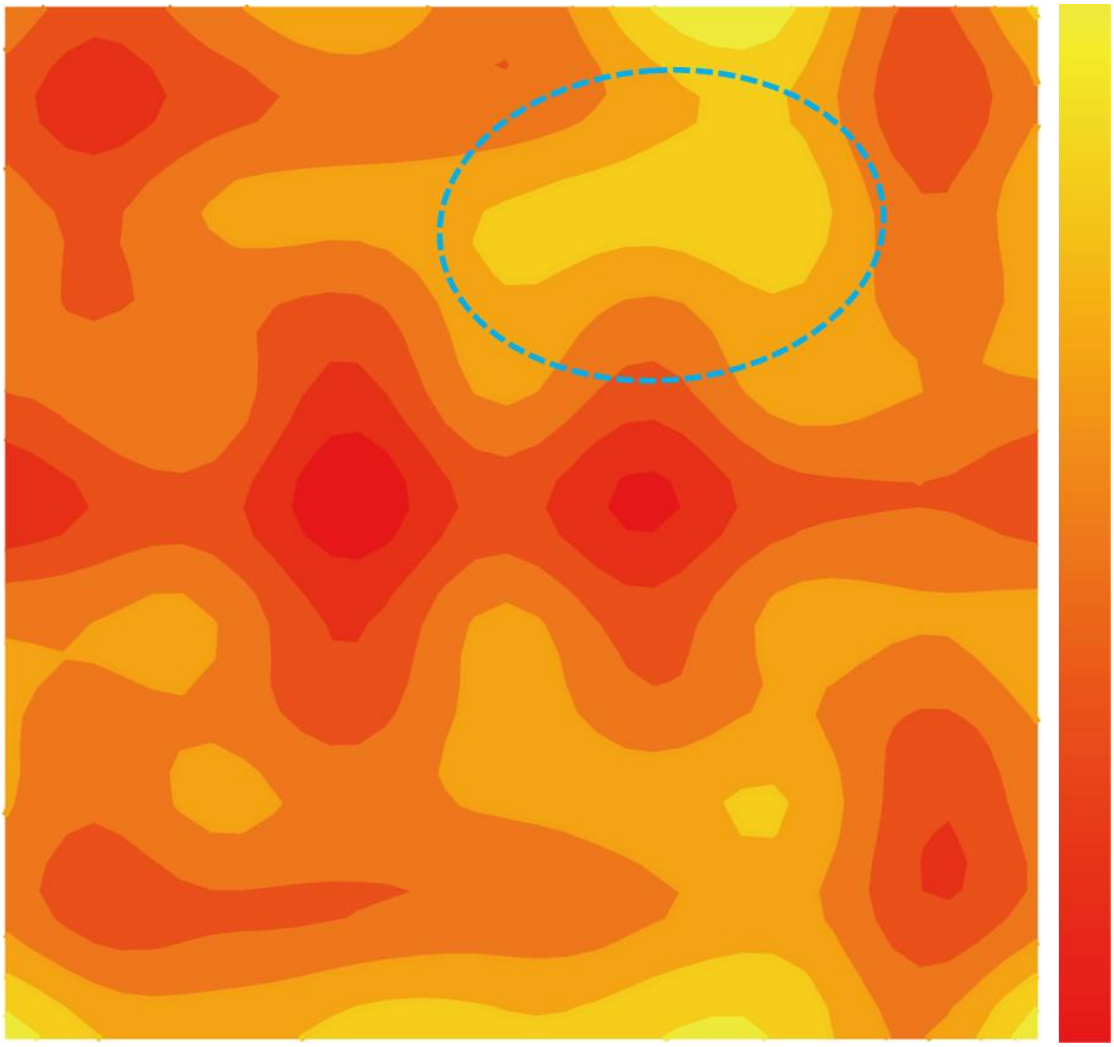

Supplementary Fig. 19 | Potential information of the catalytic material obtained via DPC-STEM corresponds to NCO_{δ}.

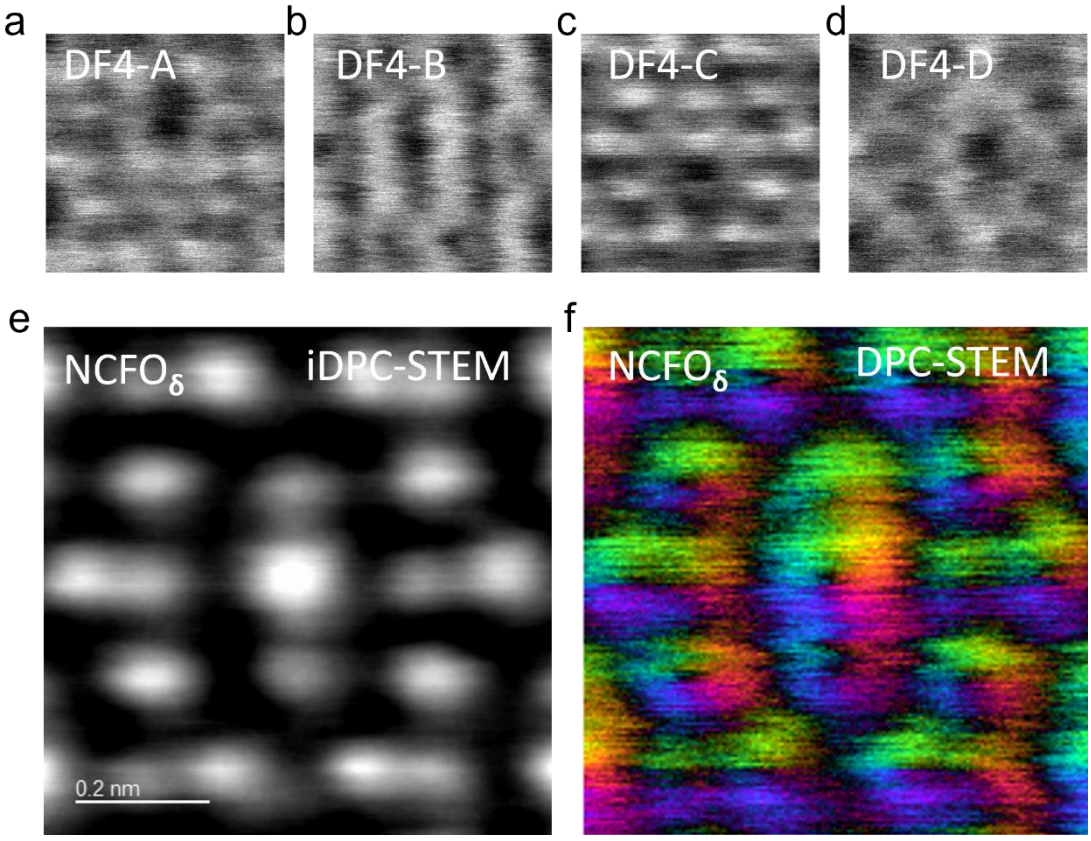

Supplementary Fig. 20 | DPC-STEM characterization of the NCFO$_\delta$ catalyst in the [110] direction. a–d. Images obtained from the quadrant detectors. **e.** iDPC-STEM image calculated from the quadrant detector images. **f.** DPC-STEM image calculated from the quadrant detector images.

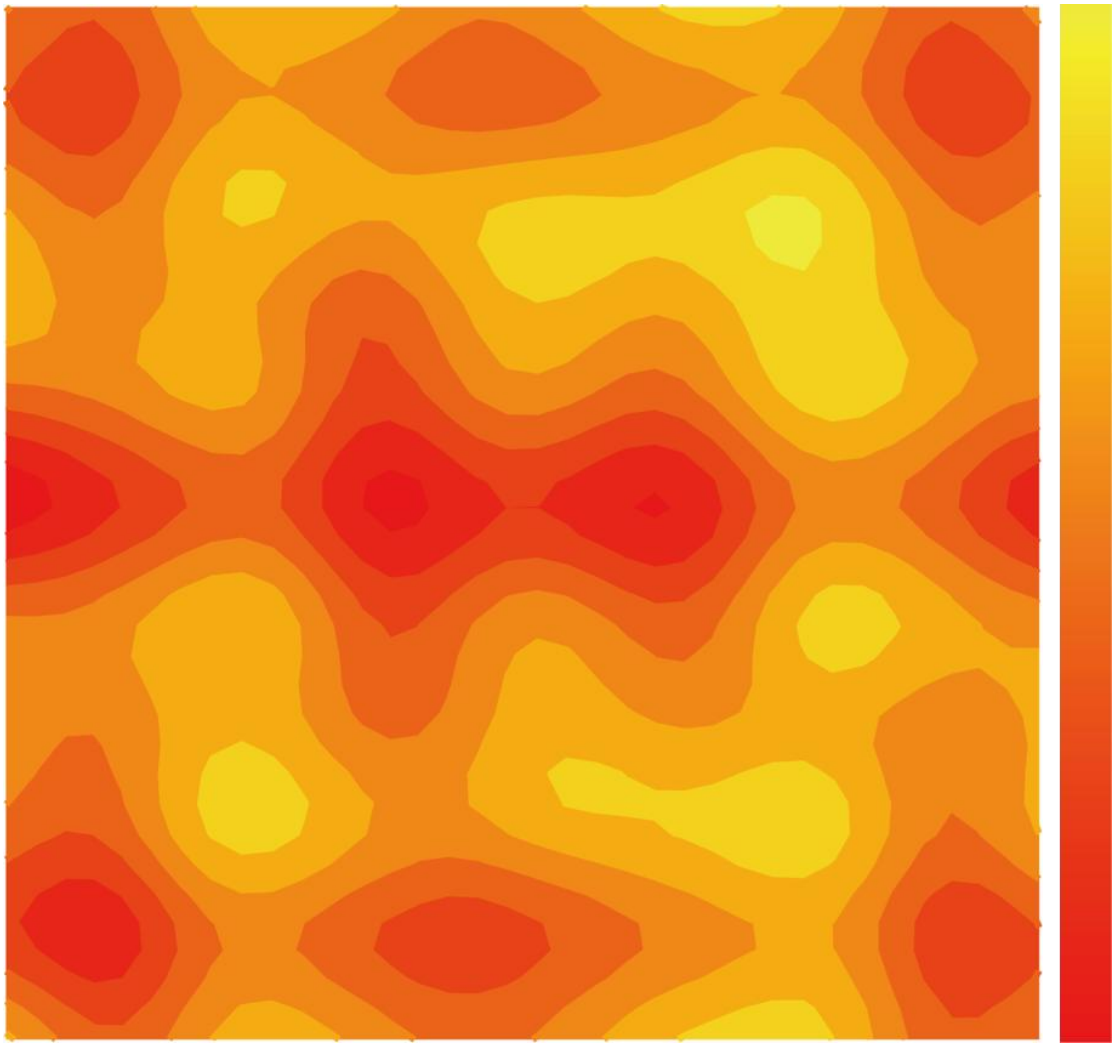

Supplementary Fig. 21 | Potential information of the catalytic material obtained via DPC-STEM corresponds to $NCFO_{\delta}$.

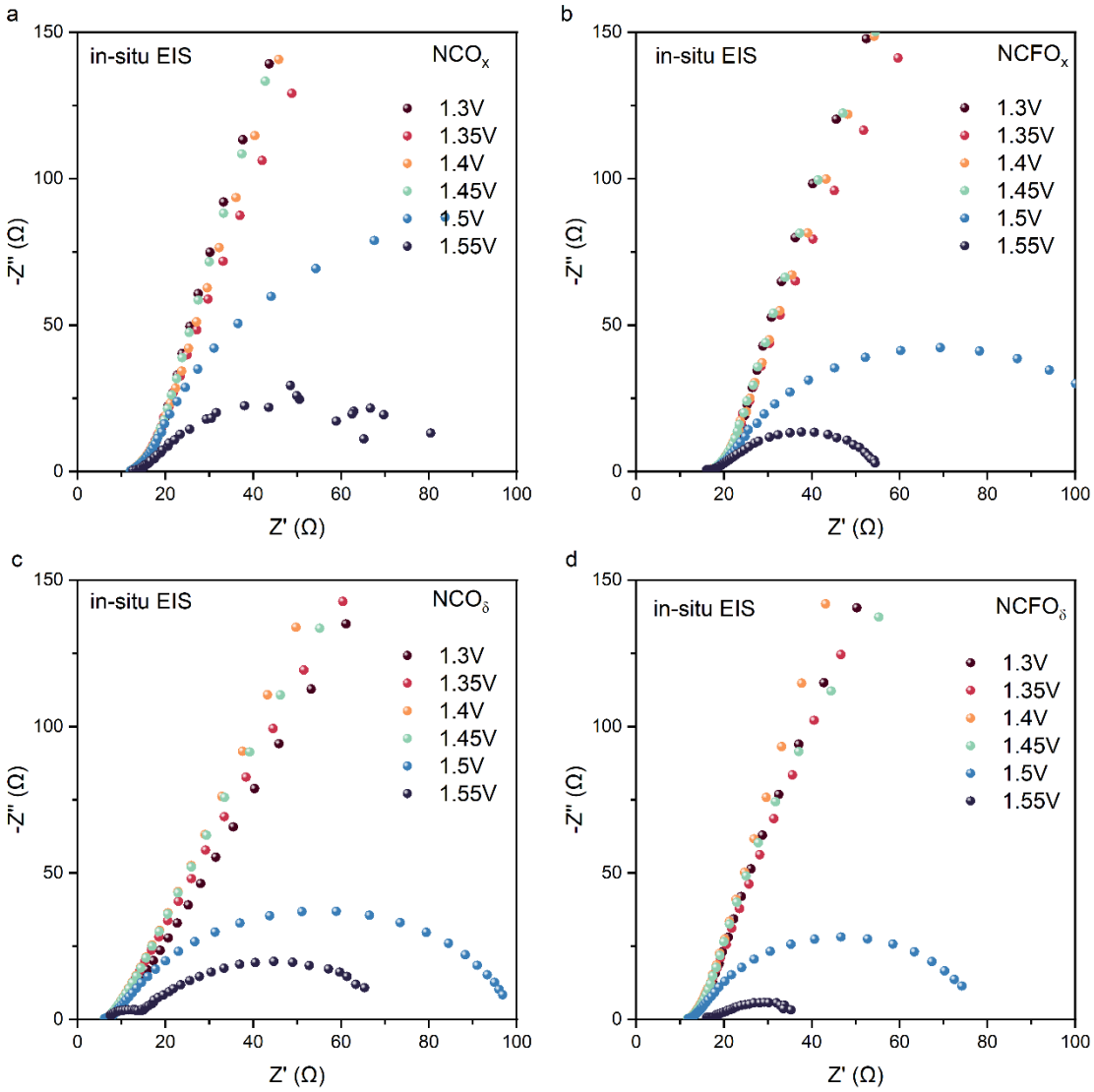

Supplementary Fig. 22 | *In-situ* EIS plots of catalysts. a NCO_x. **b** $NCFO_x$. **c** NCO_δ. **d** $NCFO_\delta$.

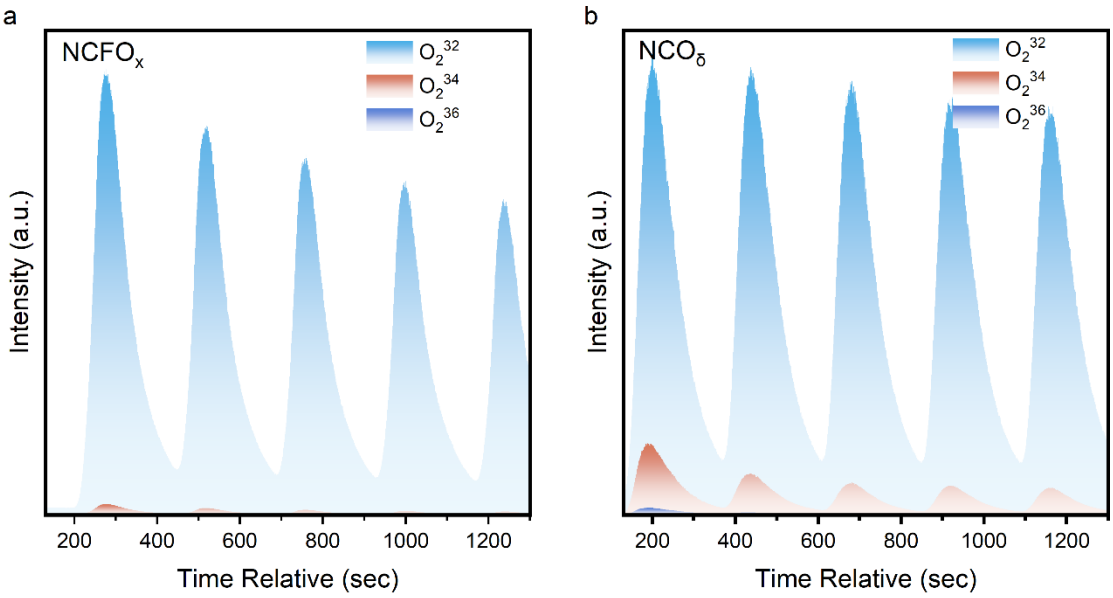

Supplementary Fig. 23 | DEMS signals of O_2^{32}, O_2^{34} and O_2^{36} of catalysts from the reaction products cycled in $H_2{}^{18}O$ aqueous KOH electrolyte. a. $NCFO_x$. **b.** NCO_δ.

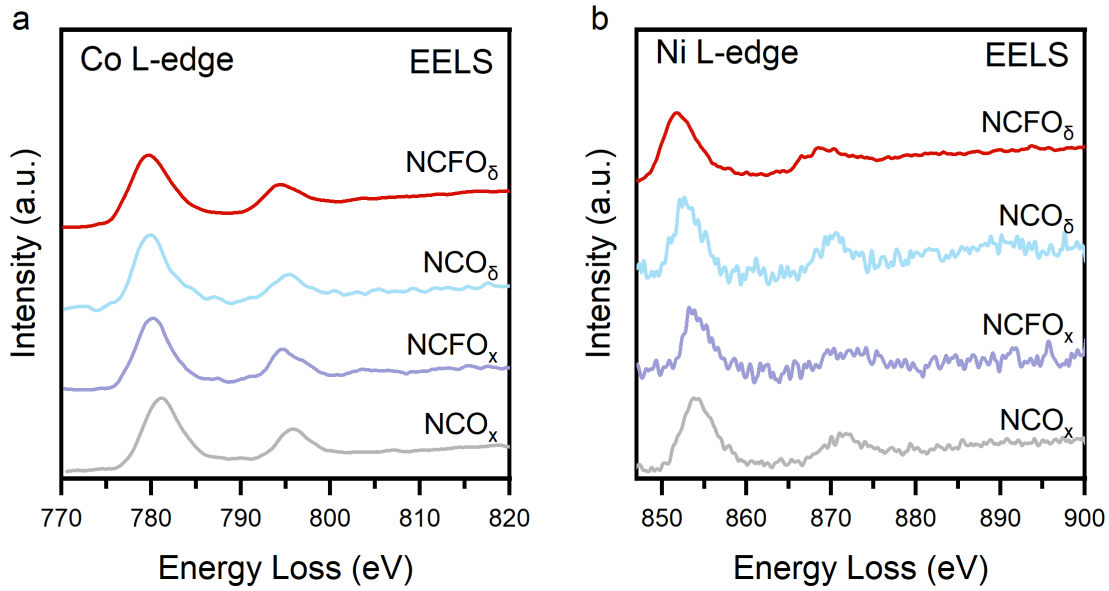

Supplementary Fig. 24 | EELS spectra of Co L-edge and Ni L-edge in catalytic materials.

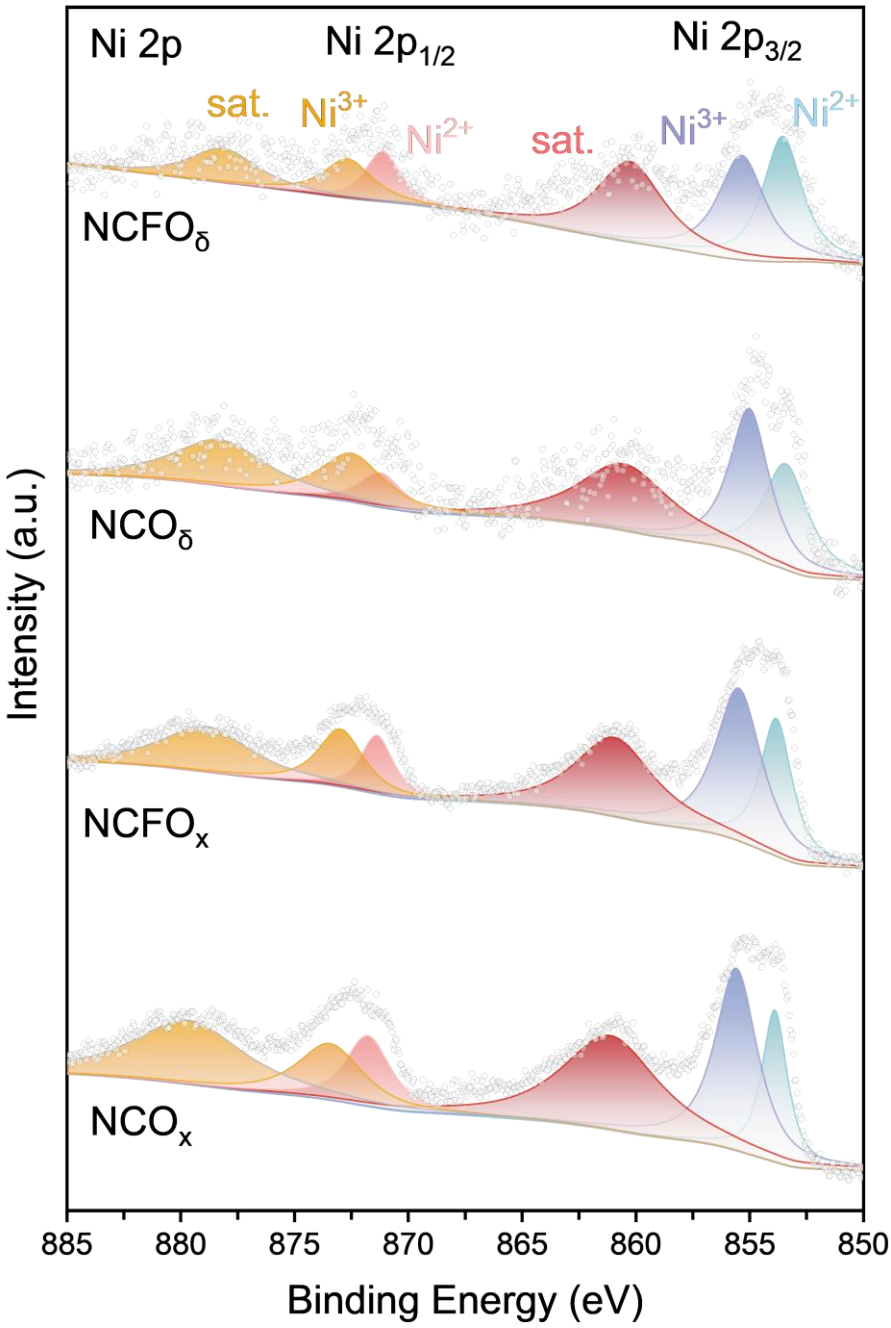

Supplementary Fig. 25 | The XPS spectra of Ni 2p in NCO_x, $NCFO_x$, NCO_δ and $NCFO_\delta$.

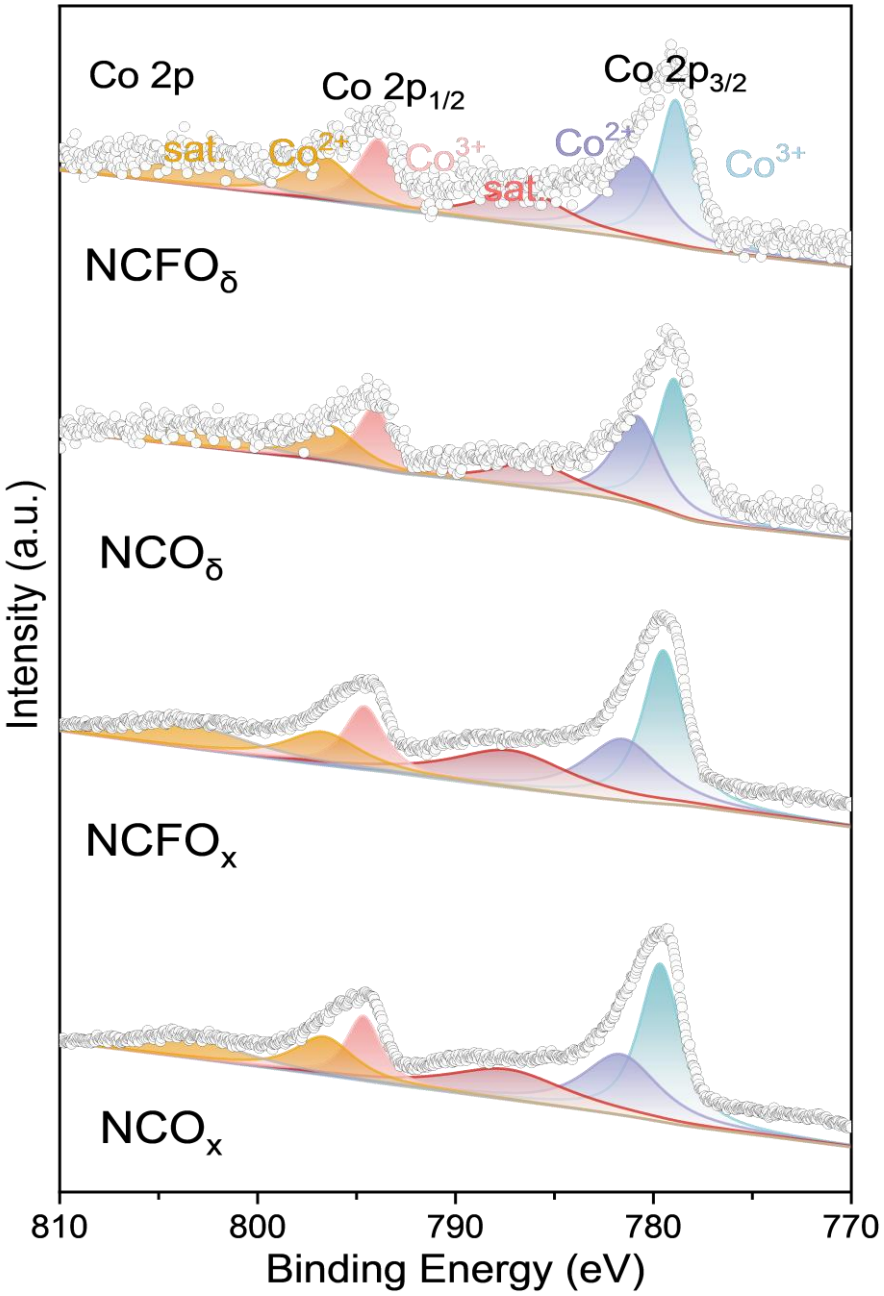

Supplementary Fig. 26 | The XPS spectra of Co 2p in NCO_x, $NCFO_x$, NCO_δ and $NCFO_\delta$.

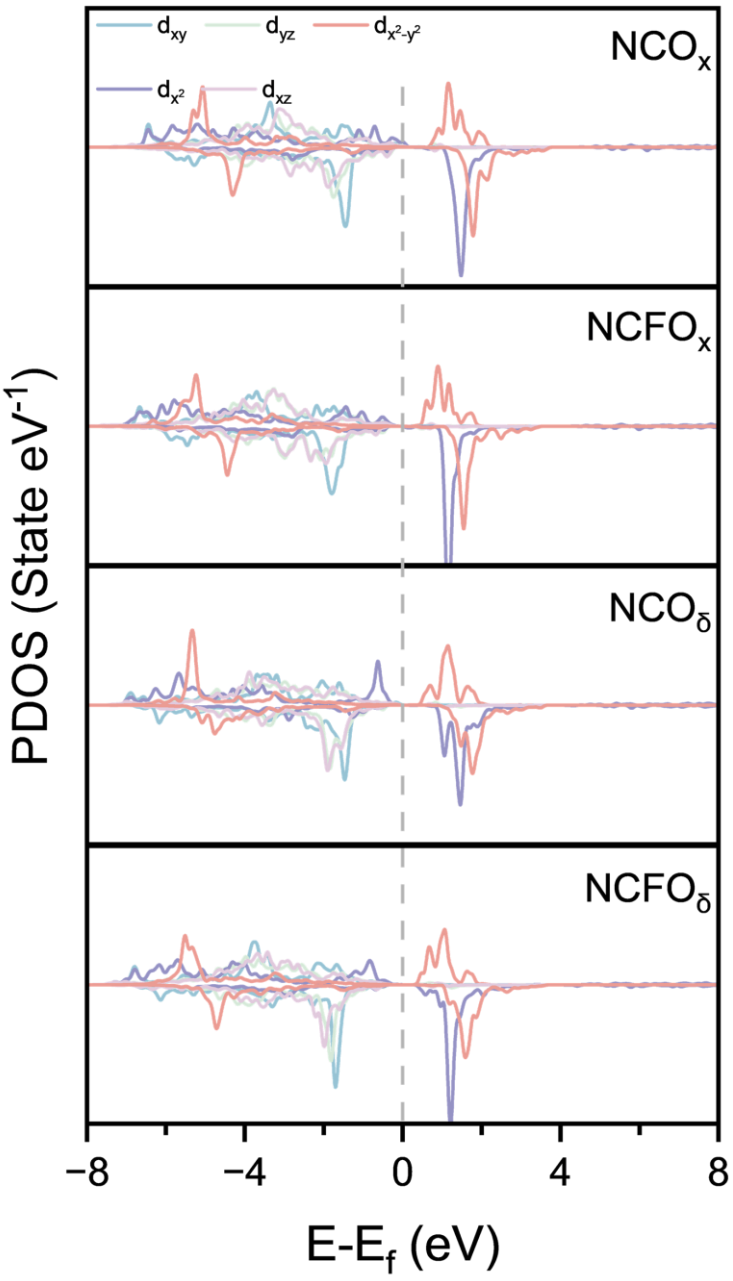

Supplementary Fig. 27 | PDOS diagram of the Ni element in catalytic materials.

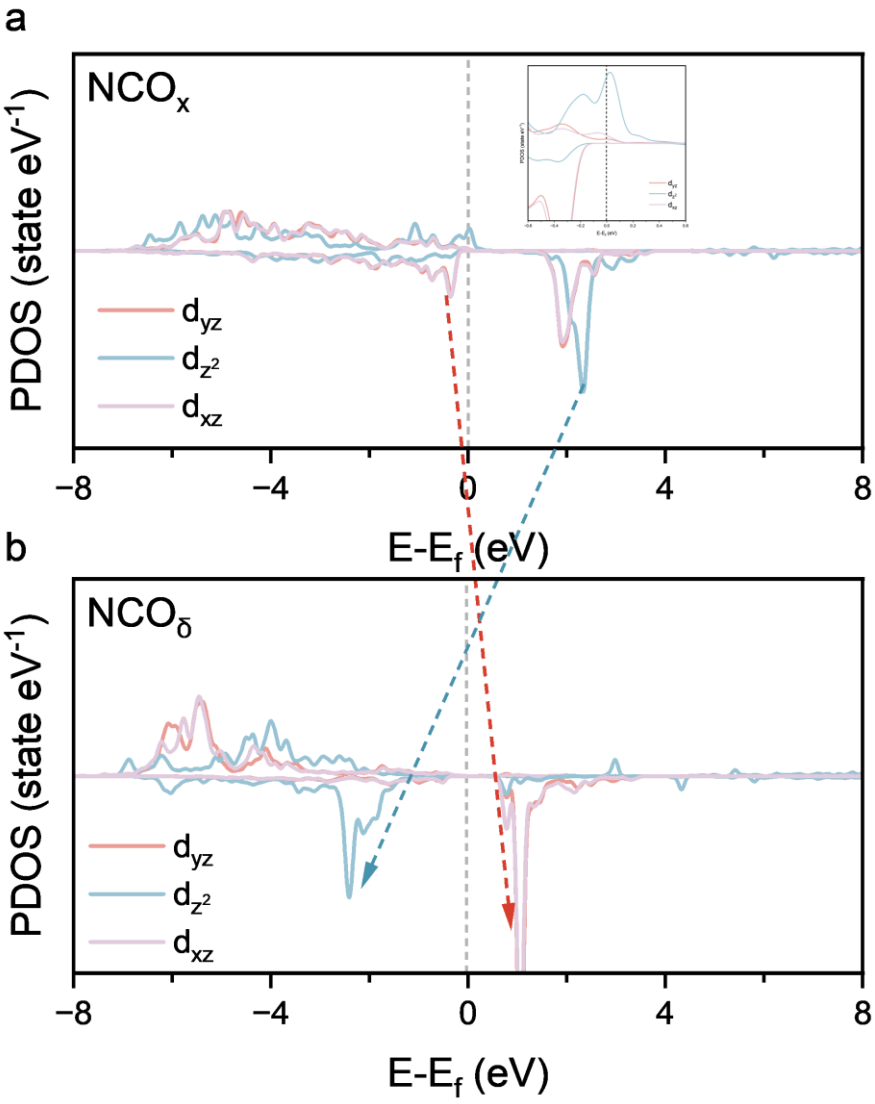

Supplementary Fig. 28 | PDOS diagrams of the d_{yz}, d_{z^2}, and d_{xz} orbitals for Co element in NCO_x and NCO_δ. **a.** NCO_x. The illustration shows a close-up near the Fermi level. **b.** NCO_δ.

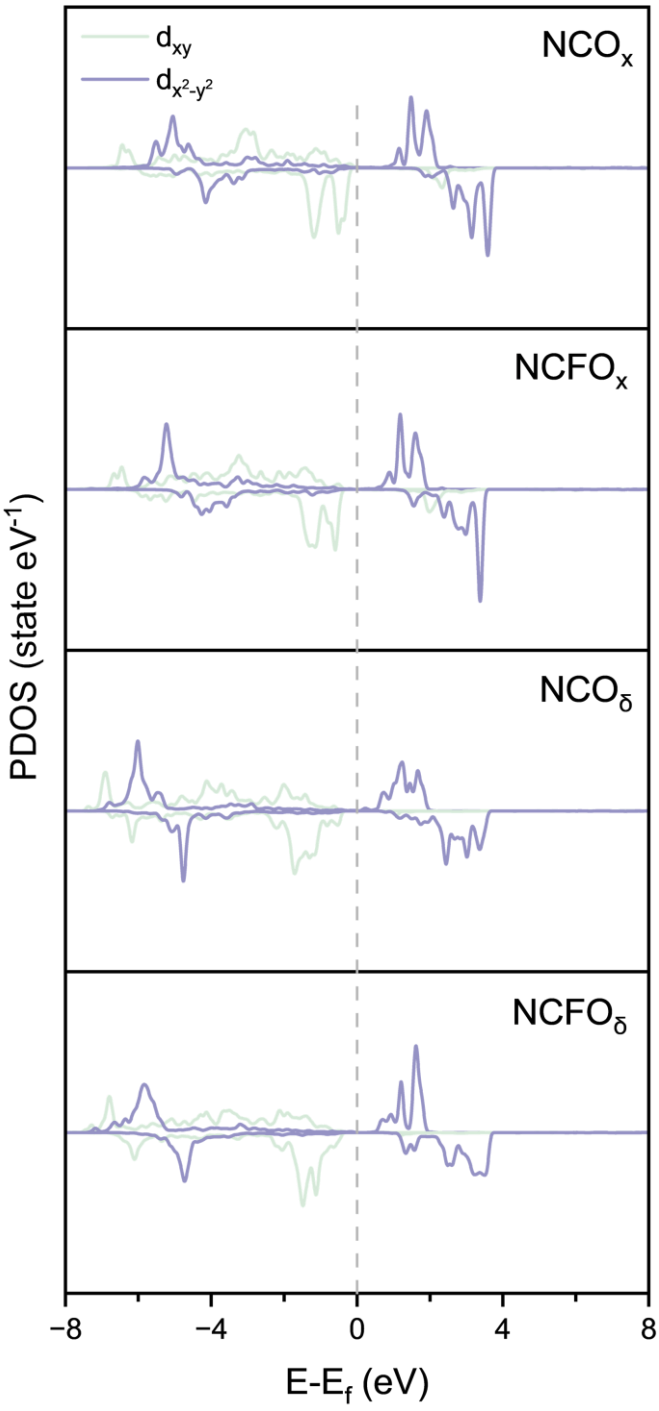

Supplementary Fig. 29 | PDOS diagram of the d_{xy} and $d_{x^2-y^2}$ orbitals for Co element in catalytic materials.

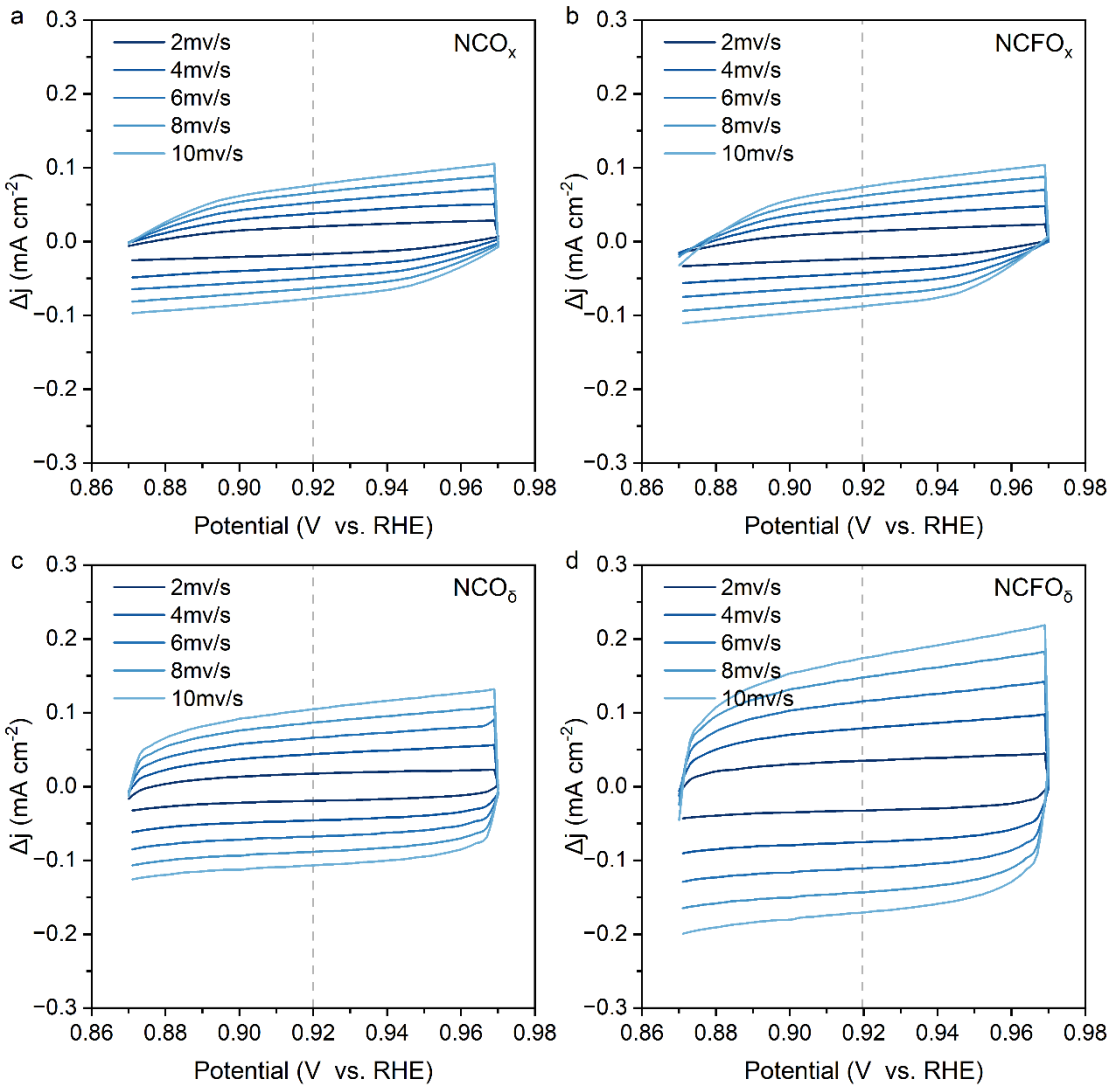

Supplementary Fig. 30 | CV curves at different scan rates. a. NCO_x. **b.** $NCFO_x$. **c.** NCO_δ. **d.** $NCFO_\delta$.

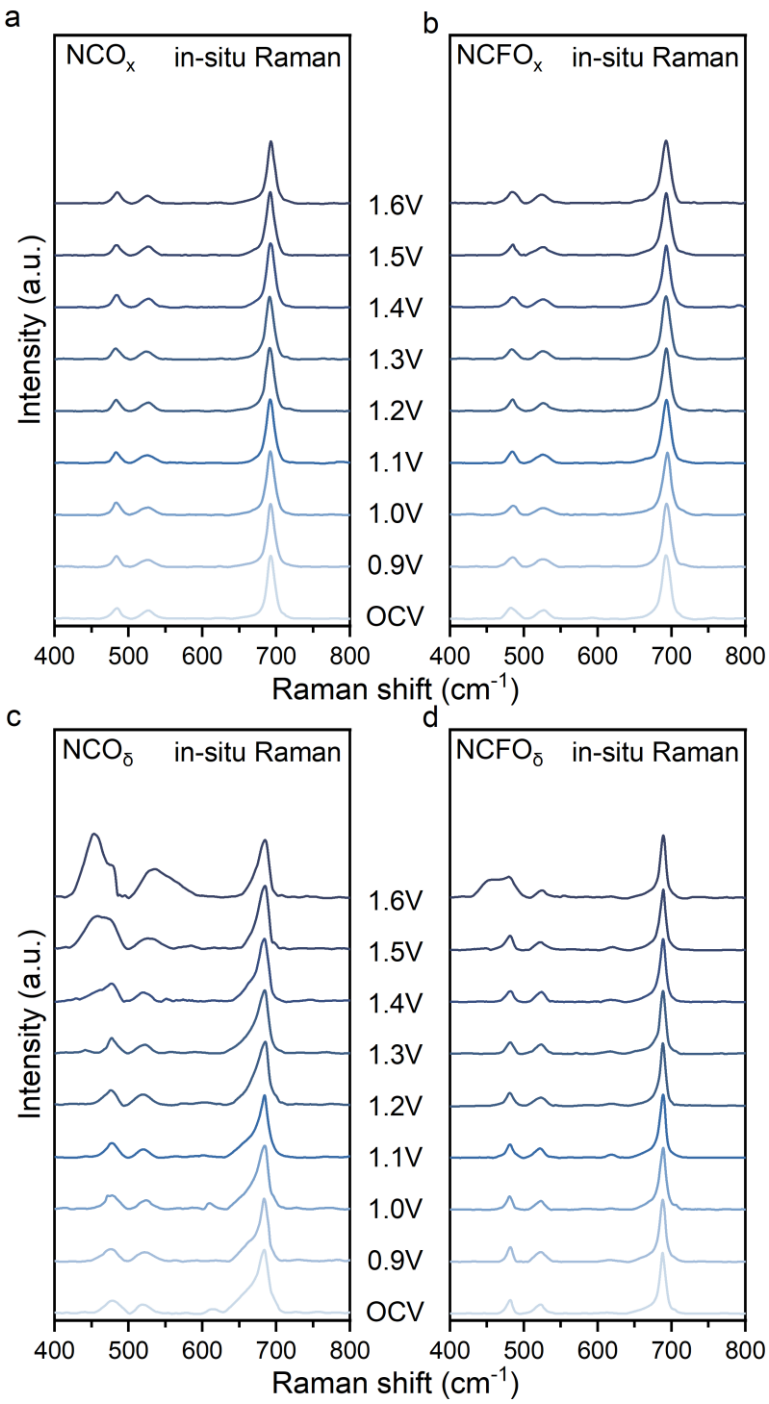

Supplementary Fig. 31 | *In-situ* Raman spectroscopy of catalysts. a. NCO_x. **b.** $NCFO_x$. **c.** NCO_δ. **d.** $NCFO_\delta$.

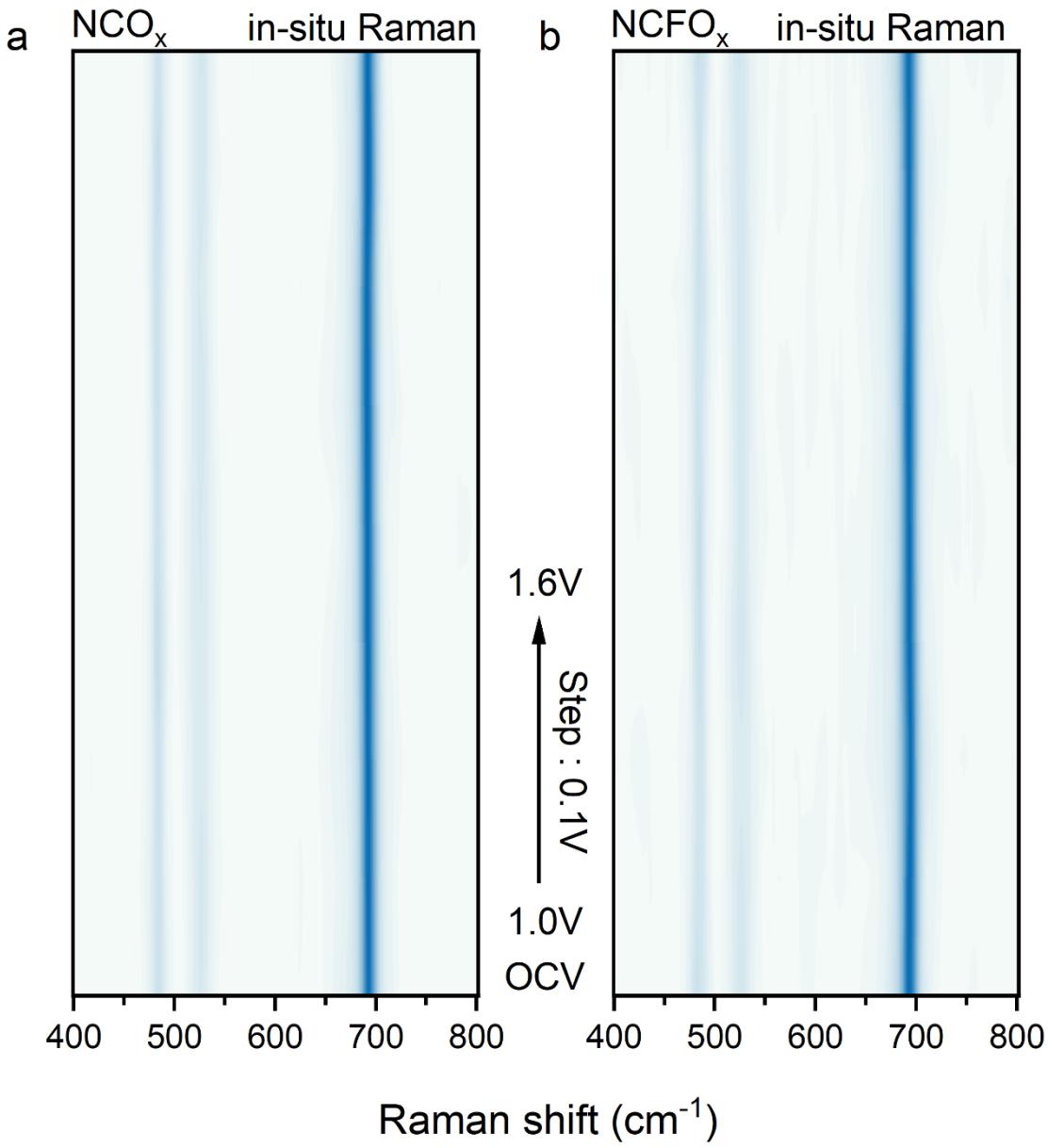

Supplementary Fig. 32 | *In-situ* Raman spectroscopy of catalysts. a. NCO_x. **b.** $NCFO_x$.

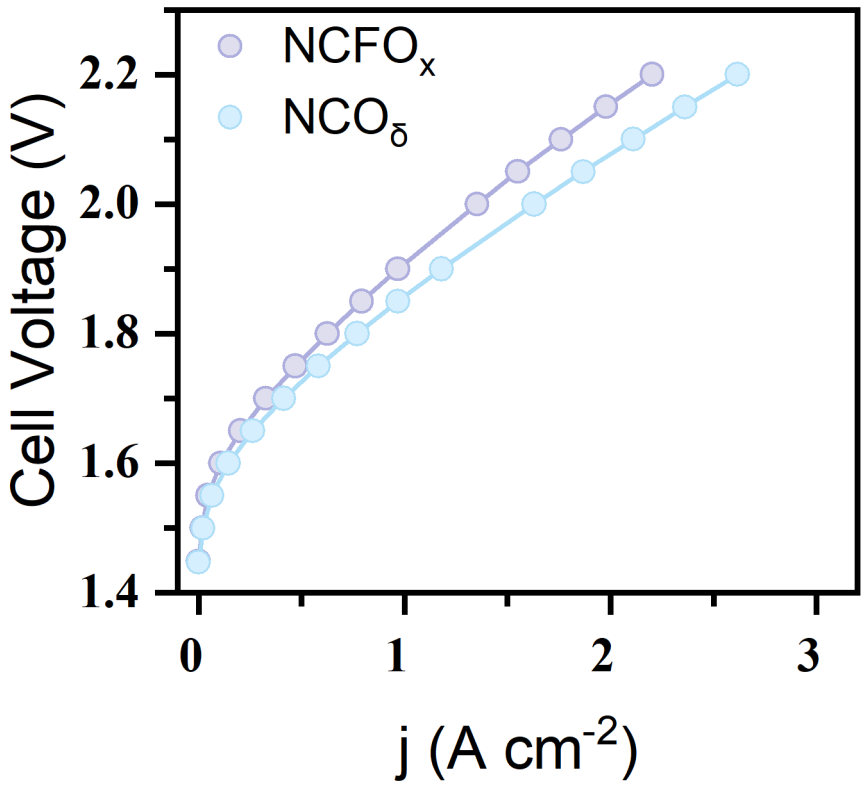

Supplementary Fig. 33 | Polarization curve of the AEM membrane electrode assembly (MEA) composed of $NCFO_x$ and NCO_δ materials at 80°C.

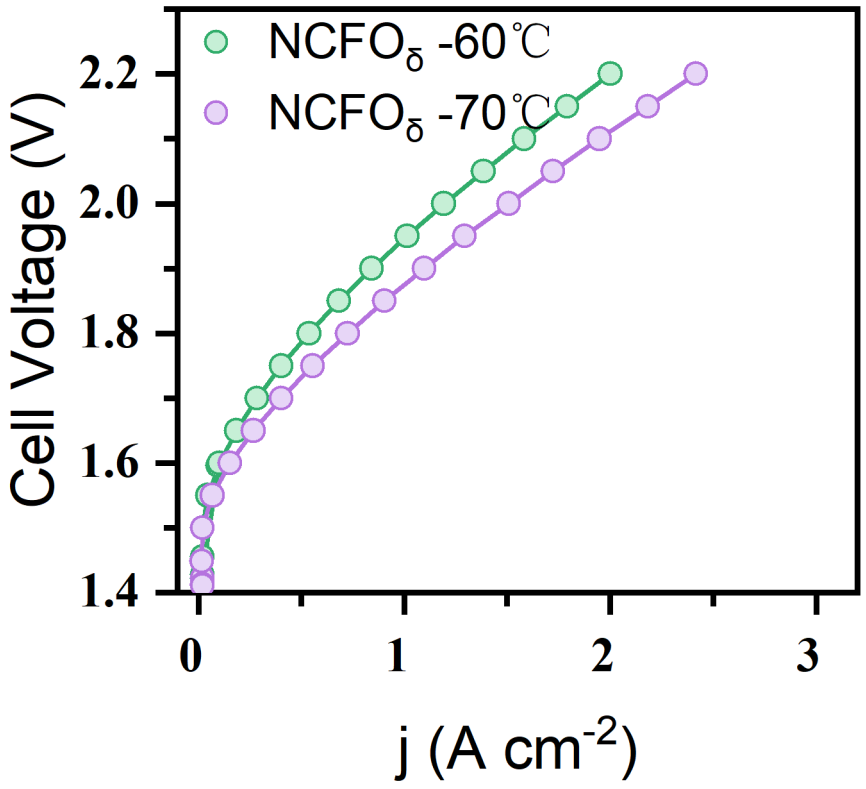

Supplementary Fig. 34 | Polarization curve of the AEM membrane electrode assembly (MEA) composed of $NCFO_\delta$ at 60°C and 70°C.

Supplementary Tables

Supplementary Table 1. The O 1s XPS peak fitting calculations yielded the H_2O, $O_{vacancy}$, and $O_{Lattice}$ content on the catalyst surface.

Peak	Area of H_2O (%)	Area of $O_{vacancy}$ (%)	Area of $O_{Lattice}$ (%)
NCO_x	14.18628426	43.25594624	42.5577695
$NCFO_x$	12.02262445	44.04312358	43.93425197
NCO_δ	17.77532634	53.40448783	28.82018583
$NCFO_\delta$	14.5292774	55.66480897	29.80591363

Supplementary Table 2. O_2^{32} and O_2^{34} and O_2^{36} contents of the catalyst obtained from DEMS data, along with the O_2^{34}/O_2^{32} ratio representing the AEM mechanism and the $O_2^{36}/O_2^{32}+O_2^{32}+O_2^{32}$ ratio representing the LOM mechanism.

Samples	DEMS				
	O_2^{32} (%)	O_2^{34} (%)	O_2^{36} (%)	O_2^{34}/O_2^{32} (%)	$O_2^{36}/O_2^{32}+O_2^{32}+O_2^{32}$ (%)
NCO_x	97.04	2.81	0.15	2.90	0.15
$NCFO_x$	98.24	1.72	0.05	1.75	0.05
NCO_δ	90.94	8.37	0.69	9.21	0.69
$NCFO_\delta$	93.48	6.16	0.36	6.59	0.36

Supplementary Table 3. The calculated content of Ni^{3+} and Ni^{2+} on the catalyst surface obtained from the fitting results of the Ni 2p XPS peak.

Samples	$2p_{1/2}$			$2p_{3/2}$		
	Area of sat. (%)	Area of Ni^{3+} (%)	Area of Ni^{2+} (%)	Area of sat. (%)	Area of Ni^{3+} (%)	Area of Ni^{2+} (%)
NCO_x	20.54581778	10.58668162	9.297386729	26.23117812	22.08935788	11.24957786
$NCFO_x$	15.41697414	9.856827067	7.296481589	23.84067164	26.76365623	16.82538933
NCO_δ	16.7486354	11.99609662	5.835690727	24.04260938	22.63097846	18.74598942
$NCFO_\delta$	10.98870113	9.149790061	8.38295198	25.15500364	23.16691114	23.15664205

Supplementary Table 4. The calculated content of Co^{3+} and Co^{2+} on the catalyst surface obtained from the fitting results of the Co 2p XPS peak.

Samples	$2p_{1/2}$			$2p_{3/2}$		
	Area of sat. (%)	Area of Co^{2+} (%)	Area of Co^{3+} (%)	Area of sat. (%)	Area of Co^{2+} (%)	Area of Co^{3+} (%)
NCO_x	9.326777537	10.64740485	10.65430485	16.93134406	21.45792594	30.98224277
$NCFO_x$	11.89784447	10.47520795	10.9948302	19.07696842	20.24716747	27.30798148
NCO_δ	9.601483414	11.48278583	13.26025828	11.85658596	24.46439383	29.33449268
$NCFO_\delta$	12.04903365	12.26267993	13.33170396	14.14976391	22.85251935	25.3542992